EUPHOTIC IODATE PRODUCTION ALONG THE ATLANTIC MERIDIONAL TRANSECT

By

Kirsten Fentzke

A THESIS

Submitted to
Michigan State University
in partial fulfillment of the requirements
for the degree of

Geological Sciences – Master of Science

2024

ABSTRACT

The oxidized iodine species, iodate, is the most pervasive form of iodine in welloxygenated marine waters and can be tracked in carbonates as a paleo-redox proxy. Despite known marine spatial concentration variations in iodate and the reduced iodide today and temporal gradients across Earth history, the rates and mechanisms of iodate formation remain poorly understood. To quantify rates and pathways of iodine cycling, we performed ship-board tracer experiments in euphotic waters across a latitudinal transect with known gradients in iodine speciation—the Atlantic Meridional Transect spanning from the Falkland Islands to Southampton in the United Kingdom (UK) (45°S to 37°N) during March 2023. We collected samples for incubations and accompanying iodine speciation depth profiles (5-500 meters) from 11 stations along the transect. All incubation sets were spiked with radioactive ^{129}I ($t_{1/2} \sim 15.7$ My) as iodide and were performed at two depths capturing the 7% and 1% light levels, thus tracking the deep chlorophyl maximum (DCM). Quantified rates varied with depth and location, with northern (spring) locales at 1% light showing the highest activity. Importantly, most locations exhibited no significant iodate production. Iodate formation from iodide is inferred from only one location based on increases in iodate ¹²⁹I/¹²⁷I ratios. At other locations, decreases in iodate ¹²⁹I/¹²⁷I ratios imply that alternative sources—likely the recycling of intermediates—are an important factor for iodate production. Ultimately, our survey reveals significant variability in iodate formation pathways in Atlantic euphotic waters, which have implications for improving models of iodine cycling and refining the paleo-redox proxy. Future research should focus on further elucidating mechanisms and explore seasonal and regional variations that drive iodine cycling dynamics in marine environments.

TABLE OF CONTENTS

INTRODUCTION	1
BACKGROUND	5
METHODS	9
RESULTS	14
DISCUSSION	28
CONCLUSION	
BIBLIOGRAPHY	44
APPENDIX	49

INTRODUCTION

Iodine is the most abundant trace element in Earth's oceans, and both influences and tracks the biogeochemical cycling of carbon and oxygen. For example, iodine is redox-sensitive, and partitioning between the reduced and oxidized endmember—iodide (I⁻) and iodate (IO₃⁻), respectively—tracks redox dynamics in global oxygen minimum zones. Exploiting this modern redox relationship, the abundance of iodine in carbonate rocks—which incorporate the oxidized iodate—has been used as proxy for reconstructing ancient oxygen availability across geologic time (Lu et al., 2010). In addition, marine phytoplankton both assimilate iodine and reduce iodate to iodide in euphotic waters (Hepach et al., 2020). The resulting assimilated iodine contributes to iodine biogeochemical cycling in sediments and the water column (Hepach et al., 2020). Iodide generated at the sea surface further interacts with and degrades tropospheric ozone and is a major component of atmospheric ozone cycling models (Carpenter et al., 2013; Chance et al., 2014; Luhar et al., 2017). Importantly, the formation and persistence of iodate, the most abundant and ubiquitous marine iodine species today, is an essential component for quantitative integration and application of iodine cycling within each of these fields; yet there are little-to-no observational constraints on iodate formation rates, pathways, and mechanisms, including spatiotemporal controls. This project seeks to address this knowledge gap by quantifying iodate formation rates and pathways in a diversity of marine settings across Atlantic Euphotic waters from the Falkland Islands to the UK (45°S to 37°N).

While aspects of the iodine cycle are not well understood, the distribution patterns of marine iodine are well known. Primarily, iodine exists in two main forms: iodide and iodate, which are both dissolved and generally sum to 400-500 nM total iodine (Campos et al., 1996). Iodate comprises nearly 100% of total iodine outside of the ocean surface and marginal upwelling zones. Within these settings, iodine speciation showcases a dynamic distribution influenced by various environmental factors. First, iodate is reduced to iodide, often quantitatively, in oxygen-deficient or reducing conditions (Luther, 2023; Moriyasu et al., 2020; Wong & Brewer, 1977). Second, iodate reduction to iodide occurs in euphotic waters during primary production (Chance et al., 2014; Spokes & Liss, 1996). Importantly, while iodate still predominates in euphotic settings, iodide persists even under fully oxygenated conditions (Chance et al., 2014). This suggests that I oxidation in marine waters is likely slow and not directly related to O₂ (1.5-560 nM/yr) (Campos et al., 1996; Edwards & Truesdale, 1997; Hardisty et al., 2020; He et al., 2013; Hughes, et al.,

2021; Luther, 2023; Truesdale et al., 2001; Žic & Branica, 2006). Importantly, while a trend of elevated euphotic iodide transitioning to nearly total iodate at depth can be seen globally, this trend is exacerbated in stratified low latitude settings (Chance et al., 2014). This suggests that, in addition to *in situ* cycling, seasonal mixing trends with underlying iodate-rich waters may also drive trends in euphotic iodine speciation. Iodine cycling thus involves several interrelated biological, chemical, and physical processes.

A key iodine cycling process in euphotic waters is the conversion of iodate (IO₃) to iodide (I) by phytoplankton and bacteria (Hepach et al., 2020). In addition to the direct reduction of iodate, phytoplankton also assimilate iodine during their growth. This iodine is eventually released back into the marine environment when the phytoplankton die and decompose. However, some iodine appears to be absent when mass balance calculations are performed in these productive zones. This discrepancy can be partly explained by the temporary storage of iodine within the cells of phytoplankton, which is released upon their senescence and decay. This delayed release of iodine may account for the observed shortfall in these calculations (Hepach et al., 2020).

While processes driving iodate reduction are better understood—both in oxic euphotic waters and oxygen deficient zones—there is uncertainty regarding the rates and pathways of iodate formation. Specifically, because iodate comprises nearly 100% of total iodine outside of the ocean surface and terrestrial and seafloor margins—where major internal and external fluxes of iodide are concentrated—the implication is that iodate production in the ocean is likely widespread. However, the redox disequilibria indicated from the long-term accumulation of iodide implies that iodide oxidation may be extremely slow, at least in some or most settings.

Beyond potentially slow rates, another key inhibitor for quantifying iodate formation is uncertainty regarding the formation pathways and mechanisms. This knowledge gap limits our ability to replicate iodate production reactions in the lab or to target marine settings most likely to host such reactions. To date, there is some evidence that iodate production may be facilitated by some combination, but not likely exclusive to, reaction with reactive oxygen species (ROS), manganese, and during nitrification. ROS, such as superoxide (O2) and hydrogen peroxide (H2O2), can oxidize iodide (T) to iodate (IO3) directly or indirectly via intermediate species like hypoiodous acid (HOI) and iodine monoxide (IO)(Luther, 2023). ROS production is often associated with biological activity, especially in surface waters where photosynthesis and respiration occur (Luther, 2023). Nitrification, a microbial process involving the oxidation of

ammonia (NH₃) to nitrite (NO₂) and then to nitrate (NO₃), may also indirectly contribute to iodate production (Hughes et al., 2021). Nitrate produced during nitrification can react with iodide, leading to the formation of iodate as a byproduct. While these pathways have been addressed in laboratory settings, they have not been demonstrated under ambient marine conditions. Directly observing these processes across an Atlantic transect will allow for deeper understanding of how and where iodate forms or its interactions within biogeochemical cycles.

One implication of slow iodide oxidation rates is that mixing processes may play an important role in the distribution of iodine species in marine settings. Understanding how vertical mixing sources affect iodate/iodide distribution at the sea surface is crucial (Wadley et al., 2020). Horizontal and vertical mixing, driven by factors like wind, tides, and currents, can homogenize iodine concentrations within water masses (Wadley et al., 2020). Horizontal mixing occurs along oceanic currents and eddies, leading to the dispersal of iodine species over large spatial scales (Wadley et al., 2020). Vertical mixing, on the other hand, involves the exchange of water masses between different depths, impacting the vertical distribution of iodine (Chance et al., 2020). Vertical diffusion refers to the movement of substances, including iodine species, across vertical gradients in water properties such as temperature, salinity, and density. This process is driven by molecular diffusion and turbulent mixing, particularly near boundaries like the thermocline and halocline. Vertical diffusion can influence the transfer of iodine between surface and deeper waters, affecting speciation patterns (Qi et al., 2023). The combined effects of mixing and vertical diffusion have several implications for iodine speciation and distribution. Mixing processes can homogenize iodine concentrations horizontally, leading to relatively uniform distributions over large oceanic regions. However, vertical gradients in iodine speciation may still exist, especially near oceanic boundaries and transition zones (Moriyasu et al., 2020). Mixing and diffusion facilitate the transport of iodine species across oceanic regions, including lateral transport along current pathways and vertical transport across water column layers. This transport can influence the spatial variability of iodine concentrations and speciation. Vertical diffusion contributes to the establishment of vertical profiles of iodine species within the water column. For example, in regions with strong vertical gradients in biological activity or redox conditions, vertical diffusion can lead to distinct vertical distributions of iodide and iodate (Miwa et al., 2020). Changes in iodine speciation and distribution due to mixing and diffusion can impact marine ecosystems, including

phytoplankton communities that utilize iodine for metabolic processes. Vertical nutrient fluxes driven by mixing can also influence nutrient availability and primary production in surface waters.

Recent research has quantified both iodide oxidation and iodate formation rates via novel tracer approaches. Specifically, recent studies have used a 129-iodine tracer approach in shipboard seawater incubations to track iodate formation rates from iodide and intermediates (Hardisty et al., 2020; Schnur et al., 2024; Ştreangă et al., 2023). Each of these studies focused on different regions and conditions, leading to unique findings. Hardisty et al. (2020) investigated the iodate formation rates in Martha's Vineyard Sound, USA. Their results indicated that biological activity may catalyze iodate formation. In contrast, Schnur et al. (2024), conducted their study in the Sargasso Sea and did not observe iodate formation, which they attributed to lower biological activity and different chemical conditions. This study highlighted how regional variations in environmental factors such as temperature and nutrient availability can significantly influence iodine cycling. Ştreangă et al. (2023) focused on subtropical regions in the North Pacific Ocean, where they determined that intermediate iodine species may be particularly important in driving iodate formation. Importantly, each of these local studies had different observations, pointing to a need for large surveys to determine broader trends in the pathways of iodate production.

To investigate large-scale trends in the pathways and rates of iodate production via iodide and intermediates, we performed shipboard ¹²⁹I radiotracer incubations under ambient seawater conditions during the Atlantic Meridional Transect (AMT-30) in February to March of 2023. With a half-life of ~15.7 Ma, ¹²⁹I is useful as a tracer on timescales of decades or less (Hardisty et al., 2020, 2021). This study aims to fill the knowledge gap in understanding iodine's chemical reactions and rates in seawater, which is crucial for marine science and has implications for the cycling of other essential elements like carbon, dissolved oxygen, and ozone.

BACKGROUND

AMT-30 (Figure 1) and the broader AMT program offer a unique platform for studying iodine speciation, particularly iodate production, by combining extensive field observations, incubation experiments, tracer techniques, and a comprehensive multi-disciplinary approach. These efforts contribute to advancing our knowledge of marine biogeochemistry and its implications for global nutrient cycles (Aiken et al., 2000; Rees et al., 2015). By conducting sampling along a latitudinal gradient, the AMT-30 enables direct observation of changes in iodine speciation and production over large spatial and temporal scales. This latitudinal approach is crucial for understanding how oceanographic conditions, such as temperature, salinity, and nutrient availability, influence iodine dynamics. The AMT program has a long history of repeated expeditions, providing a valuable dataset with temporal continuity (Rees et al., 2015). Long-term observations allow for the detection of trends, seasonal variations, and a deeper understanding of how this study fits into the broader set of accumulated data.

Spanning from high latitudes in the North Atlantic to low latitudes in the South Atlantic, the AMT covers a diverse range of marine environments. One of the significant contributions of the AMT program is the study by Aiken et al. (2009), which offers a decadal assessment of phytoplankton pigments and functional types across the Atlantic Ocean. Utilizing AMT data from 1995 to 2005, this study focused on the distribution and variability of phytoplankton communities, revealing significant spatial and temporal patterns. The research highlighted how different phytoplankton functional types and pigments varied across the Atlantic, with shifts linked to changes in oceanographic conditions and nutrient availability. This comprehensive assessment underscores the AMT's role in providing long-term, high-resolution data essential for mapping key phytoplankton groups and elucidating their roles in ocean biogeochemical cycles. Picoplankton are dominant in oligotrophic waters, nanoplankton in mesotrophic waters, and microplankton in eutrophic waters. There was low inter-annual variability in total chlorophyll a across provinces, with some evidence of perturbations where cruise track differences were thought to be responsible for those changes (Aiken et al., 2009). This long-term perspective is crucial for understanding how phytoplankton dynamics are influenced by environmental changes and how these dynamics, in turn, affect marine ecosystems.

Further advancing our understanding of oceanic processes, Aiken et al. (2017) synthesized data on the environmental responses of the North and South Atlantic Sub-Tropical Gyres over two

decades of AMT observations. This synthesis elucidates long-term trends in oceanographic conditions, such as temperature and nutrient concentrations, and their impacts on marine productivity and community structure. The paper reveals several key findings about the North and South Atlantic Sub-Tropical Gyres (NAG, SAG). AMT data define gyre boundaries, with lowvelocity flow within the gyres and higher velocities at their edges. The surface layer is nutrientdepleted with low chlorophyll a (Chla) biomass, while the deeper chlorophyll maximum (DCM) is nutrient-replete but light-limited. Seasonal variations show surface Chla peaks in mid-winter due to the "Light Effect," and DCM Chla reaches its maximum in mid-summer but declines as sunlight decreases. Two modeling approaches extend remote sensing (RS) observations to greater depths and simulate seasonal cycles, addressing gaps in AMT sampling. Differences between the NAG and SAG include significant dust input in the NAG and varying trends in sea surface temperature and physical properties (Aiken et al., 2017). The study emphasizes the need for additional data from January and July and suggests that future research could benefit from expanding networks like Argo and bio-Argo for improved 3D visualizations and data coverage. The study underscores the value of continuous, long-term data in detecting subtle changes in oceanic conditions and in understanding the broader implications for marine biogeochemistry and ecosystem health.

The efficiency of particulate organic carbon (POC) export and its transfer to the deep ocean has been another focal point of AMT research, as explored by Henson et al. (2012). This study investigates global patterns in the export of POC and its subsequent fate in the ocean interior. High-latitude regions with diatom dominance showed high export efficiency but low transfer efficiency, indicating labile organic matter, while low-latitude regions with effective microbial recycling had low export efficiency but high transfer efficiency, suggesting more refractory organic matter. The study concludes that ecosystem structure, rather than the presence of CaCO₃, is the key factor controlling the efficiency of the biological carbon pump (Henson et al., 2012). The findings highlight the variability in carbon export efficiency across different regions of the Atlantic and emphasize the role of POC in the global carbon cycle. Understanding these patterns is critical for assessing the ocean's role in sequestering atmospheric CO₂ and for evaluating the potential impacts of climate change on carbon cycling.

Additionally, the role of micro-phytoplankton in photosynthesis, primary production, and potential export production has been addressed by Tilstone et al. (2017). Their research provides

detailed insights into how micro-phytoplankton contribute to primary production and nutrient cycling in the Atlantic Ocean. They found that micro-phytoplankton contributed about 30% to total primary production (PP) in the top 50 meters of the North Atlantic Drift (NADR) and North Atlantic Tropical (NATL) regions, but this contribution dropped to 15–30% in the West Tropical Atlantic (WTRA) and South Atlantic Tropical (SATL) regions. In the central NATL, the contribution was less than 15%, increasing to around 20% at the boundaries with SATL and WTRA (Tilstone et al., 2017). The study reveals the importance of different phytoplankton size classes in mediating carbon and nutrient fluxes, thereby influencing overall marine productivity and biogeochemical cycles.

The AMT program's long-term observational data are invaluable for detecting seasonal variations and understanding the broader implications of marine biogeochemical processes. Henson (2014) emphasizes the significance of these long-term records in advancing our knowledge of ocean biogeochemistry and its interactions with global nutrient cycles. The ability to track trends and changes over extended periods is crucial for assessing the impacts of both natural variability and anthropogenic influences on marine systems. The AMT program provides a unique and comprehensive platform for studying marine biogeochemistry across a wide range of environmental conditions. The program's extensive spatial and temporal coverage enables researchers to investigate complex marine processes and their interactions with global nutrient cycles. Through the integration of field observations, experimental data, and long-term records, the AMT program continues to contribute valuable insights into the dynamics of marine ecosystems and their responses to environmental changes.

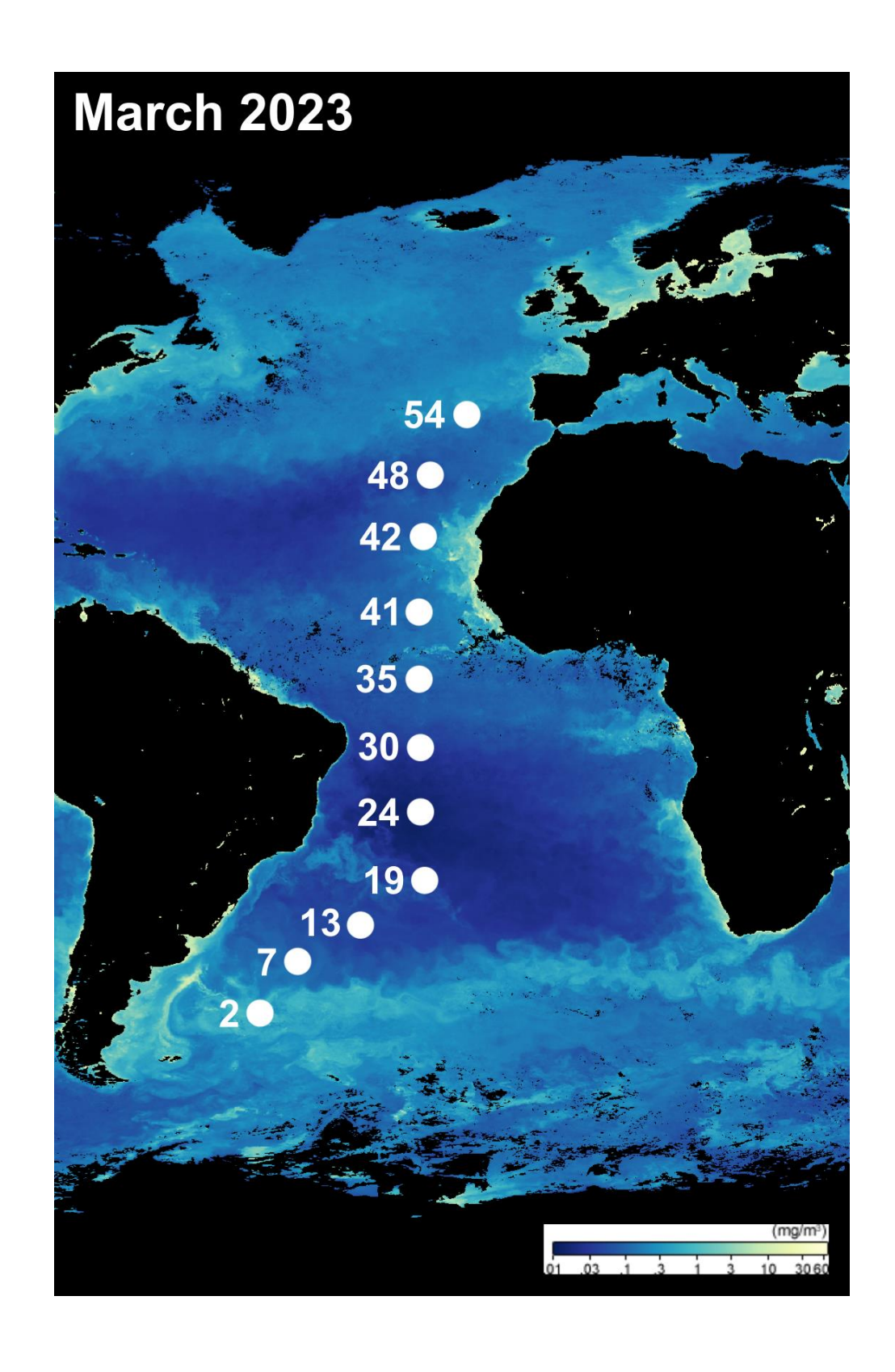


Figure 1. Surface chlorophyll values with select AMT-30 stations from February and March of 2023.

METHODS

3.1 Sample Collection

Seawater samples were collected via a CTD (Conductivity, Temperature, and Depth) rosette deployed on a cable to a maximum depth of 500 m during the AMT-30 transect cruise (Table 1). Depth profile samples from the solar noon CTD Niskin bottles were taken every three days at 11 of the 54 total stations, with 12 samples per cast (250mL each) ranging from 5m to 500m depth for a total of 132 samples for iodine speciation analysis along the transect. Samples were filtered to remove bacteria and other particles through 0.2µm filters with 0.8µm pre-filters (AcropakTM 1500 Supor Capsule, Pall Corporation) using a Masterflex pump and then placed into opaque 60mL bottles and frozen at -20°C (Campos et al., 1996; Moriyasu et al., 2023).

Additionally, larger volume samples (1-3L) were collected from depths corresponding to light levels of 7% and 1% (DCM). The iodine isotope (¹²⁹I⁻) spike was added to the larger volume first to homogenize the iodine speciation and respective isotope ratio before aliquoting into replicates. The larger volumes were spiked to a concentration of 70nM ¹²⁹I⁻ solution (t_{1/2} = 15.7 My) (Eckert and Ziegler Isotope Products[©]) (Hardisty et al., 2020, 2021; Schnur et al., 2024). Notably, the isotope spike included a NaI carrier, which included ¹²⁷I⁻, so total I⁻ added was approximately 140 nM (¹²⁹I/¹²⁷I of I⁻ ~1). Similar to previous analogous applications (Hardisty et al., 2020, 2021; Schnur et al., 2024; Ştreangă et al., 2023), there is also a small amount of ¹²⁹IO₃⁻, which allows for isotopic ratio analyses of the t₀ timepoints for iodate and then subsequent changes can be interpreted to reflect *in situ* processes.

Each spiked carboy was split into triplicate 250mL incubations (Hardisty et al., 2020b). Incubations occurred within on-deck flow-through incubators with screens replicating the light levels of the sample depths. Samples for t₀ were immediately subsampled after adding the spike. All subsamples were filtered at 0.2μm to end interaction with biology, put into amber high-density polyethylene (HDPE) Nalgene bottles, and frozen at -20°C. All (t₀, t₁, t₂) subsamples were ~60 ml. Subsamples of 60mL were taken after 1.5-3 days. Incubation conditions were monitored for pH and taxonomic analysis onboard. All taxonomic analysis were conducted on board by Glen Tarran from Plymouth Marine Laboratory (Rees, 2023; Tarran et al., 2006). All samples were stored frozen (at -20°C) until analysis at Michigan State University.

3.2 Spectrophotometry

Iodate concentrations from select depth profiles were quantified using a technique for spectrophotometric measurement of iodate adapted from Jickells et al., (1988). This method involves reacting seawater iodate with an excess of potassium iodide (KI) and sulfamic acid, which generates triiodide (I₃-) in a reaction specific to iodate. Potassium iodate is known to degrade quickly over time; therefore, a fresh 10% KI solution was prepared daily for analysis. Sample intensity at specific wavelengths was recorded by a VWR 3100 PC UV-Vis Scanning Spectrophotometer equipped with UV-Vis Analyst software. Reusable Fisherbrand® Semi-Micro Quartz Cuvettes (Cat. No. 14-958-126) with a 10 mm path length were utilized for visible range (200-2500 nm) measurements. The triiodide product that is quantified via this reaction sequence exhibits a characteristic absorption spectrum with a trough around 320 nm, a peak at 350 nm, and a secondary trough at 400 nm. The iodate concentration (nM IO₃-) was calculated from these spectral features using the equation:

$$nM_{IO_3-} = \frac{(A(IO_3^-)_{350} - (A(IO_3^-)_{\sim 320} + A(IO_3^-)_{400})}{2} \times m_{standard\;curve}$$

The $m_{standard\ curve}$ variable represents the slope of a calibration curve generated from potassium iodate (KIO₃-) standards that were created using iodate additions to seawater over a range of 0-500nM. This approach, based on the specific reaction of iodate with iodide under acidic conditions to form triiodide, enabled precise quantification of iodate concentrations in these samples.

3.3 ICPMS Concentration Analysis (Column Chromatography)

An established ion-exchange chromatography protocol was employed to separate iodide (I⁻), iodate (IO₃⁻), and dissolved organic iodine (DOI) species from natural seawater samples for measurement of their concentration in AMT-30 samples from the 7% and 1% light depths (Hardisty et al., 2020, 2021; Hou et al., 1999, 2001, 2007, 2009; Moriyasu et al., 2023; Wong & Brewer, 1977). The iodide fractions were analyzed via triple-quad inductively coupled mass spectrometry (ICP-MS-TQ) to quantify iodine concentrations, as previous studies have demonstrated near-complete (~100%) recovery yields (Hardisty et al., 2020). Subsequently, these fractions were

measured for ¹²⁹I/¹²⁷I isotope ratios using multicolletor inductively coupled mass spectrometry (MC-ICP-MS). Iodate recovery yields have been shown to typically range from 90-95% (Hou et al., 1999, 2001, 2007, 2009), which is confirmed in this work as well. While this does not impact our isotope analyses, we recognize that low yields could contribute to uncertainty between triplicates for iodate concentration measurements made from this fraction for our incubations.

The iodine speciation was conducted using glass columns packed with PYREX glass wool and 1 mL of AG1-X8 resin, which were pre-cleaned to eliminate residual iodine before sample processing. Cleaning was performed by replacing seawater samples with 18.2 MΩ·cm water within a full ion chromatography separation procedure. Approximately 20 mL of each seawater sample, measured gravimetrically, was used for chromatographic separation. Iodide was eluted from the seawater matrix after iodate and DOI were released from the resin. Iodate and DOI were collected independently, but DOI was not measured. The iodate fraction was then reduced to iodide using concentrated hydrochloric acid (HCl) and 0.3 M sodium bisulfite (NaHSO3), following the methods outlined by Hardisty et al. (2020), Hou et al. (1999, 2009), Reifenhäuser & Heumann (1990), and Schnur et al. (2024). After an overnight reduction, these fractions underwent a second round of chromatography on cleaned resin for iodide elution using an 18% TMAH/2 M HNO3 eluent. The masses of the eluent and samples were measured gravimetrically to facilitate concentration calculations.

For quality control, a 200 ppb iodide solution (diluted from a $1000 \pm 4 \mu g/mL$ iodide standard in 1% tetraethylammonium (TEA) for iodide or dissolved solid KIO₃ in $18.2 \text{ M}\Omega$ ·cm water for iodate was processed through the columns alongside the samples to assess elution efficiency and yield. Two $18.2 \text{ M}\Omega$ ·cm water blanks were included for each column set to check for contamination, and at least one replicate sample was processed in each column set to evaluate reproducibility. Iodide concentrations [$^{127}I^-$] were measured using a Thermoscientific iCap triple-quad inductively coupled plasma mass spectrometer (ICP-MS-TQ) with Qtegra software version 2.10.3324.131, in both single-quad (SQ) and triple-quad (TQ) modes with O₂ reaction cell gas as outlined in Schnur et al. (2024). A Teledyne ASX 520 autosampler was used for sample introduction. Eluent was diluted with samples at 1:20 or 1:40 for subsequent ICP-MS analysis. The same matrix was used for ICP-MS rinse solutions. Data correction was performed using internal standards (In, Rh, and Cs) from Inorganic Ventures. Calibration curves and column standards were based on a $1000 \pm 4 \mu g/mL$ iodide standard in 1% TEA (Schnur et al., 2024).

3.4 Multi-Collector ICPMS (Sparge Technique)

Iodine isotope ratios (¹²⁹I/¹²⁷I) were analyzed at the Woods Hole Oceanographic Institution (WHOI) using a ThermoFinnegan Neptune MC-ICP-MS, following the method outlined in Hardisty et al. (2020) and Schnur et al. (2024). These measurements were performed on splits from the column chromatography used for ICPMS concentration analysis. Each day before sample analyses were performed, the instrument was tuned to maximize beam intensity for accuracy of the instrument. The mass spectrometer was set to monitor specific ion beams with mass/charge ratios (m/z) corresponding to Te (126, 128, 130), Xe (126, 128, 129, 130, 131, 132), ¹³²Ba, and ¹²⁷I and ¹²⁹I (Hardisty et al., 2020). The latter isotopes (¹²⁷I and ¹²⁹I) were detected by Faraday cups L3-L1 and H1-H3, with m/z 129 centered. Mass bias corrections were applied using a 500 ppb Te solution (Inorganic Ventures[©]), and potential isobaric interferences were tracked by monitoring ¹³¹Xe over the course of sample analysis.

Iodine samples were introduced into the instrument using a gas-based "sparge" method with desolvation prior to the samples entering the instrument. A 300 μ L/min quartz nebulizer was used to introduce the Ar carrier gas and Te solution, in conjunction with a standard sample cone and x-type skimmer cone (Hardisty et al., 2020, 2021). Samples (\leq 6 ml) were held in 30 ml Teflon vials fitted with pre-made "sparge caps" to allow for Ar gas flow through the vial. These vials were cleaned with 50% nitric acid at 90°C for >3 hours, rinsed with 18.2 M Ω ·cm water, and air-dried in a hood before reuse. To avoid contamination, tubing connecting the sparge caps to the Neptune intake was replaced after each use in between samples.

Before connecting a sample vial to the torch, the Ar gas flow rate was reduced to ~0.1 L min⁻¹ and the sample was purged with Ar for 1 minute. The gas flow was then increased to ~1.2 L min⁻¹ after connection. The Te signal was monitored until it stabilized (3-7 V), at which point the sample run was initiated. To induce iodine volatilization, 4 ml of concentrated 70% HNO₃ was injected upstream of the sample vial. The total volume of nitric acid and iodine eluent was kept <10 ml to prevent bubbling over and potential sample introduction into the torch. The collected data was corrected according to (Hardisty et al., 2020) to yield a final ¹²⁹I/¹²⁷I ratio and paired standard deviation (Schnur et al., 2024).

Table 1. Table of samples collected during AMT-30.

AMT-30 Station	Light			Depth	Samples
Numbers	Percentage	Latitude	Longitude	(m)	Collected
54	7%	37.783555	-18.766899	20	6
54	1%	37.783555	-18.766899	25	6
48	7%	29.266756	-23.666847	55	9
48	1%	29.266756	-23.666847	112	9
42	7%	20.683592	-24.983574	50	9
42	1%	20.683592	-24.983574	85	9
41	7%	10.416763	-25.283462	40	9
41	1%	10.416763	-25.283462	60	9
35	7%	0.916885	-25.366844	40	9
35	1%	0.916885	-25.366844	65	9
30	7%	-8.733511	-25.150113	90	9
30	1%	-8.733511	-25.150113	110	9
24	7%	-18.01677	-25.05022	100	9
24	1%	-18.01677	-25.05022	155	9
19	7%	-27.300227	-24.516787	75	9
19	1%	-27.300227	-24.516787	105	9
13	7%	-33.26678	-33.333398	60	9
13	1%	-33.26678	-33.333398	105	9
7	7%	-38.45003	-42.750142	30	9
7	1%	-38.45003	-42.750142	55	9
2	7%	-45.500052	-47.816875	15	9
2	1%	-45.500052	-47.816875	30	9
			Depth Profile		
			Samples Collected		132
			Total Samples		
			Collected		324

RESULTS

Over the course of the six-week cruise transect, variations in temperature (degrees Celsius), oxygen (µmol/kg), and fluorescence (µg/L) were observed via CTD (Figure 2). The fluorescence tracks the concentration of photosynthetic material at the base of the euphotic zone along the transect, known as the Deep Chlorophyll Maximum (DCM), which is defined here as the depth at which light has attenuated to only 1% of surface incidence. The DCM shifted in depth across the transect, being shallower at higher latitudes and deeper near the equator. The temperature plots closely followed the trends of the DCM, with higher temperatures reaching deeper into the water column near the equator and cooler temperatures at higher latitudes. The oxygen plot was homogeneous at higher latitudes in the upper 500 meters, with slightly lower oxygen concentrations near the equator associated with an oxygen deficient zone off the coast of Africa (Figure 2). Iodide depth profile plots followed a similar trend across the transect, with decreased concentrations of iodide at higher latitudes (40-15 degrees S/N) and a shift to lower values near the equator. At lower latitudes, iodide persisted deeper into the water column. These depth profiles resembled previous studies of euphotic waters, with iodide accumulation at the top of the profile decreasing with depth, while iodate increased with depth (Figure 2) (Chance et al., 2020; Moriyasu et al., 2023).

The iodate isotope ratios for the incubation are shown in Figures 3 and 4. The solid line shows the average value of the initial (t₀) triplicate samples measured. The dashed line shows one standard deviation above and below this average (Tables 2 and 3). For each incubation statistical test (t-test) was performed between each of the initial and final triplicate ratio values to establish statistical significance between t₀ and t_{final} timepoints. If the value calculated by the t-test was greater than 0.05 the significant difference between the mean of t_{initial} and t_{final} values the timepoints are not statistically different, implying no changes across the incubation. Conversely if the t-test values were less than 0.05 the timepoints are statistically different, implying changes across the incubation.

Overall, substantial variability in iodate ¹²⁹I/¹²⁷I ratios was observed across the AMT-30 transect, with the northern portion exhibiting the most pronounced fluctuations. This pattern overlaps with the northern hemisphere's spring season, suggesting potential seasonal influences on iodate formation dynamics. Within this context, three types of trends were observed: 1.) a lack of

 129 I/ 127 I of iodate variability between t_0 and subsequent samples; 2.) increase in 129 I/ 127 I of iodate between t_0 and subsequent samples; 3.) decrease in 129 I/ 127 I of iodate between t_0 and subsequent samples.

The majority of the 22 incubations exhibited no statistical significance between time points, 17 incubations show no changes between timepoints. An example of no variability is station 7 at 7% light (Figure 3). The 7% light level at Station 35 is the only example of a statistically significant positive shift. Several incubations exhibit a negative shift between the initial and final timepoints. Station 35, 41, 42, and 48 at the 1% light level show this significant decrease in the ¹²⁹I/¹²⁷I iodate between timepoints (Figure 4).

The same t-tests approach was used to determine changes in iodate and iodide isotope ratios (Figures 3, 4, 5, and 6) as well as the concentrations of iodate and iodide (Figures 7, 8, 9, and 10) during the incubations. These t-test results of all incubations are summarized in Tables 2 and 3. With the exception of Station 48 at the 1% light level, stations with statistically significant changes in the ¹²⁹I/¹²⁷I of iodate also had statistically significant changes in some combination of iodide ¹²⁹I/¹²⁷I and iodate and iodide concentration. Iodide ¹²⁹I/¹²⁷I ratios across both light depths generally did not change significantly, with only two negative shifts observed between time points at stations 35 (7%) and 7 (1%). Speciation concentrations of iodate and iodide remained consistent overall, although smaller variations were noted between the 1% and 7% light depths. Statistically significant changes in iodate concentrations were observed at the 1% light depth for Stations 30, 35, and 42, based on calculated t-test values (Figure 8). Stations 30 and 35 showed a decrease in iodate concentration between the initial and final timepoints, while Station 42 exhibited an increase (Figure 8). In contrast, only Station 7 at the 1% light depth showed a statistically significant decrease in iodide concentrations between timepoints. At the 7% light level, no statistically significant changes were detected in either iodate or iodide concentrations between the initial and final timepoints (Figures 3, 4, and 6).

The taxonomic analyses of the incubation experiments reveal that species counts remained relatively stable across all three timepoints via flow cytometry (Figure 11). While the overall populations did decrease over time, this decline is within the expected range for die-off typically observed during shipboard incubations, where removing seawater from its in-situ environment onto the ship can induce some stress on the organisms (Karl & Dore, 2001; Veldhuis & Timmermans, 2007). Despite this, the consistency in species counts suggests that the community

structure did not undergo any significant shifts, indicating a relatively stable taxonomic composition throughout the incubation period.

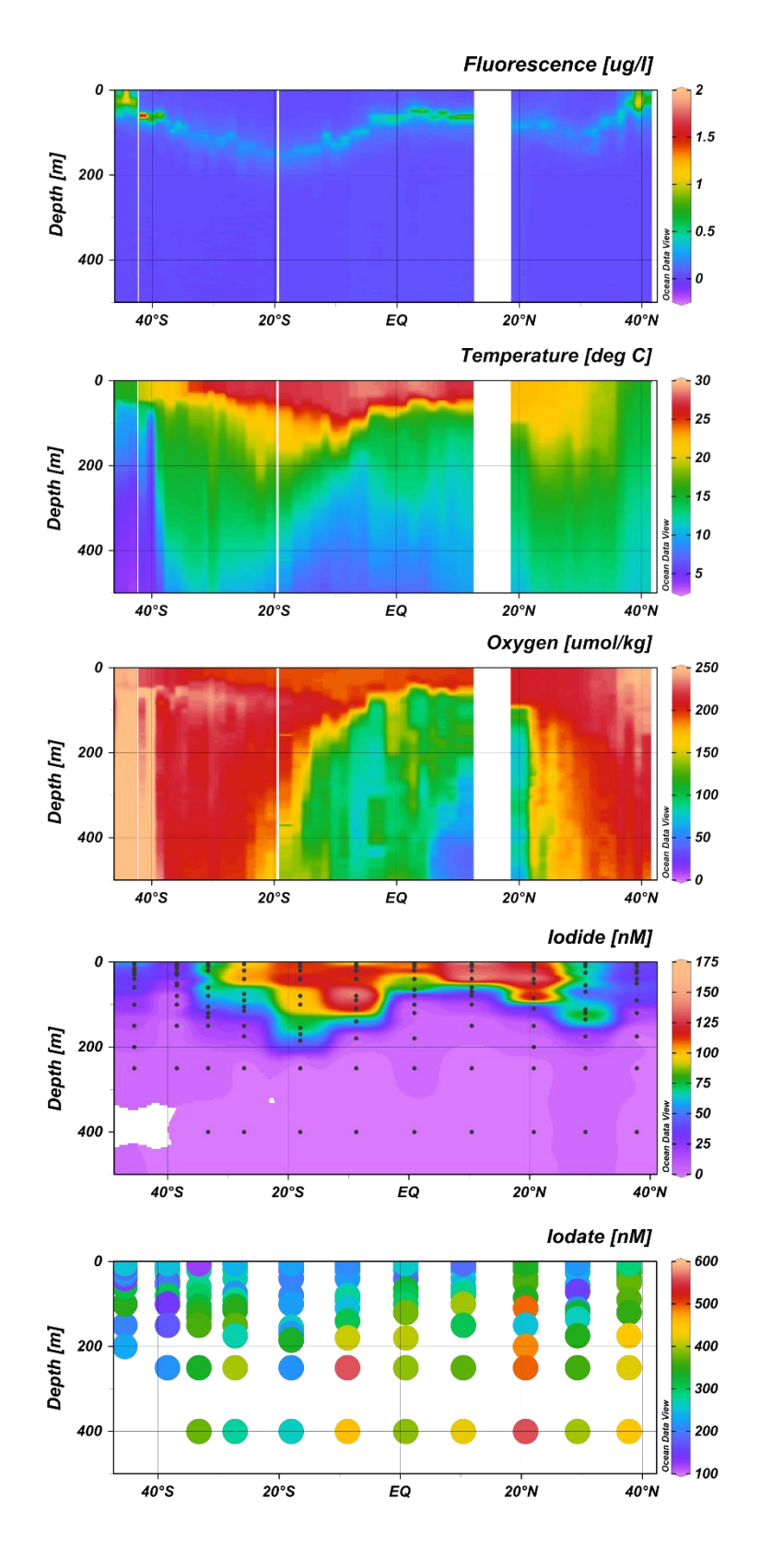


Figure 2. Ocean Data View plots of the AMT-30 transect from top to bottom: fluorescence (ug/L), temperature (degrees Celsius), oxygen (µmol/kg), iodide (nM), and iodate (nM).

Table 2. Table summarizing the results of the changes in iodate and iodide isotope ratios as well as iodate and iodide concentrations from the 7% light level between the initial and final timepoints using a t-test. A "0" means no discernable change, "+" is a positive shift, and "n/a" is not available due to insufficient data being available for that station.

7%	Ligh
Tab	ole

Station Number	Iodate Isotope Ratio	Iodide Isotope Ratio	Iodate Concentration (nM)	Iodide Concentration (nM)
54	0	0	0	0
48	0	n/a	0	0
42	0	n/a	0	0
41	0	n/a	0	0
35	+	-	0	0
30	0	n/a	0	0
24	0	n/a	0	0
19	0	n/a	0	0
13	0	0	0	0
7	0	0	0	0
2	0	0	0	0

Table 3. Table summarizing the results of the changes in iodate and iodide isotope ratios as well as iodate and iodide concentrations from the 1% light level between the initial and final timepoints using a t-test. A "0" means no discernable change, "+" is a positive shift, "-" is a negative shift, and "n/a" is not available due to insufficient data being available for that station.

1% Light Table

Station Number	Iodate Isotope Ratio	Iodide Isotope Ratio	Iodate Concentration (nM)	Iodide Concentration (nM)
54	0	0	0	0
48	-	0	0	0
42	-	0	+	0
41	-	n/a	0	+
35	-	0	-	0
30	0	n/a	-	0
24	0	0	0	0
19	0	n/a	0	0
13	0	n/a	0	0
7	0	-	0	-
2	0	n/a	0	0

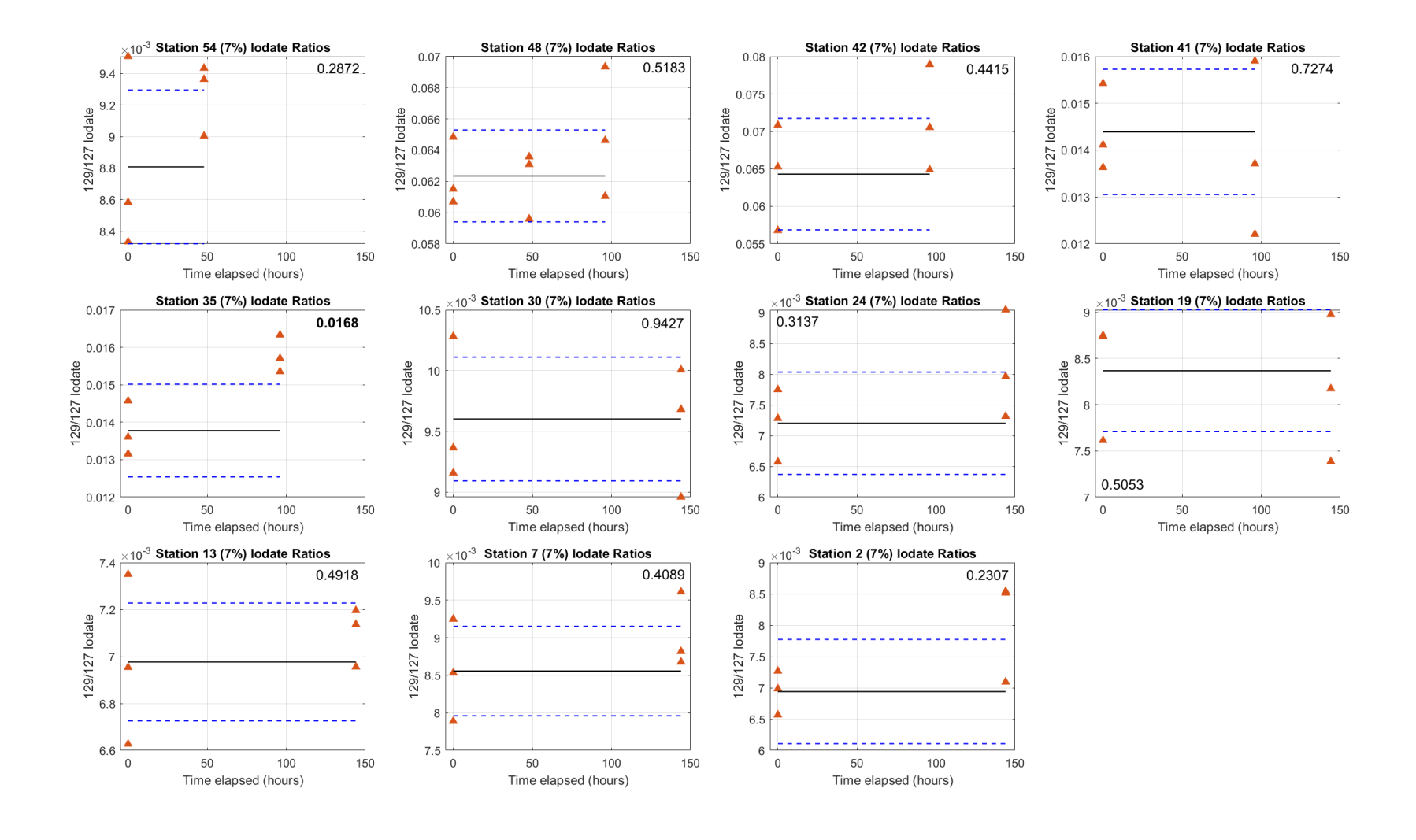


Figure 3. Plots of iodate isotope ratios from 11 stations (54 to 2) from the 7% light depth. Each plot includes every available timepoint as well as the initial average, calculated from the average of the triplicate timepoint collected at t₀ (0 hours), marked by the solid black line and one standard deviation above and below the average (dotted blue line). The value placed in the corner of each plot is the calculated p value from the performed t-tests.

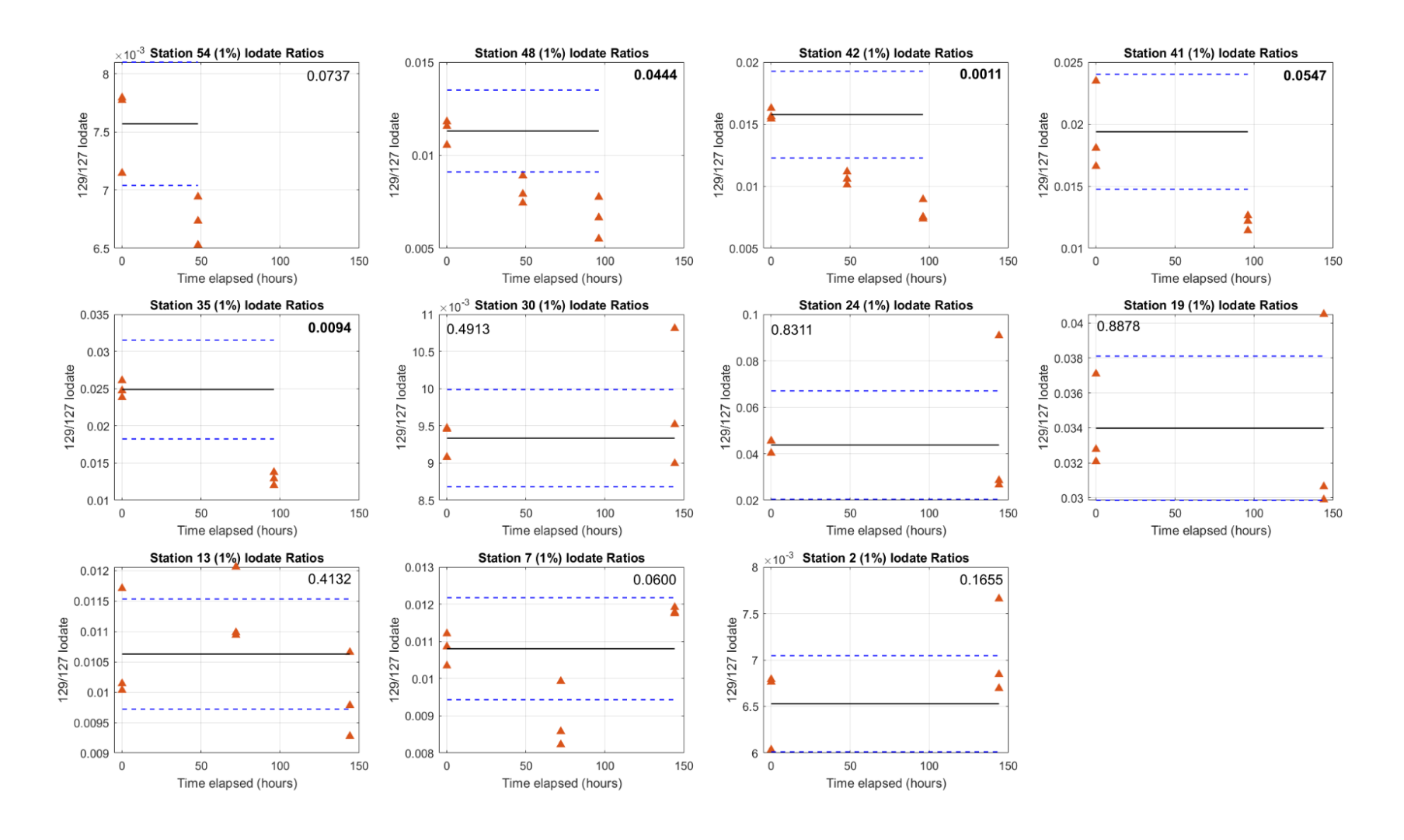


Figure 4. Plots of iodate isotope ratios from 11 stations (54 to 2) from the 1% light depth. Each plot includes every available timepoint as well as the initial average, calculated from the average of the triplicate timepoint collected at t_0 (0 hours), marked by the solid black line and one standard deviation above and below the average (dotted blue line). The value placed in the corner of each plot is the calculated p value from the performed t-tests.

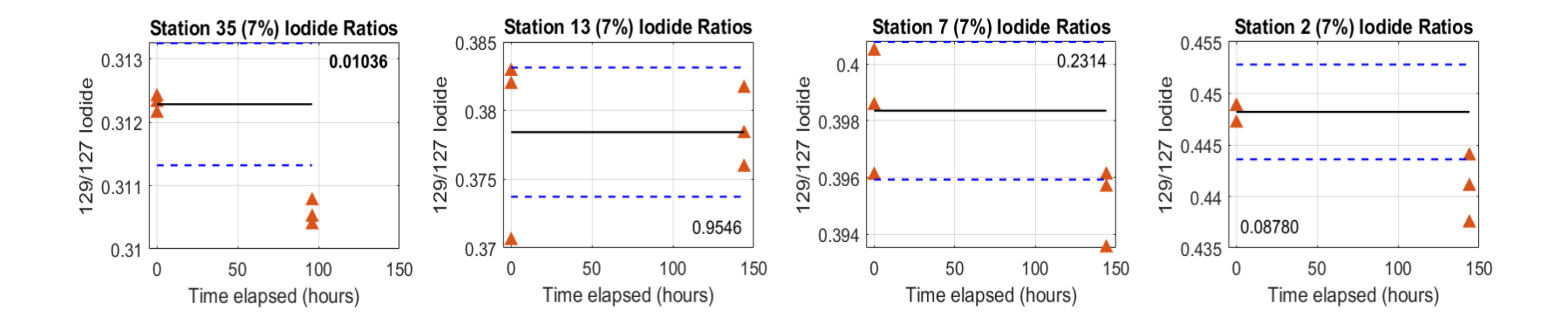


Figure 5. Plots of iodide isotope ratios from 3 stations (35, 13, 7, and 2) from the 7% light depth. Each plot includes every available timepoint as well as the initial average, calculated from the average of the triplicate timepoint collected at t_0 (0 hours), marked by the solid black line and one standard deviation above and below the average (dotted blue line). The value in the upper right corner of each plot is the calculated p value from the performed t-tests.

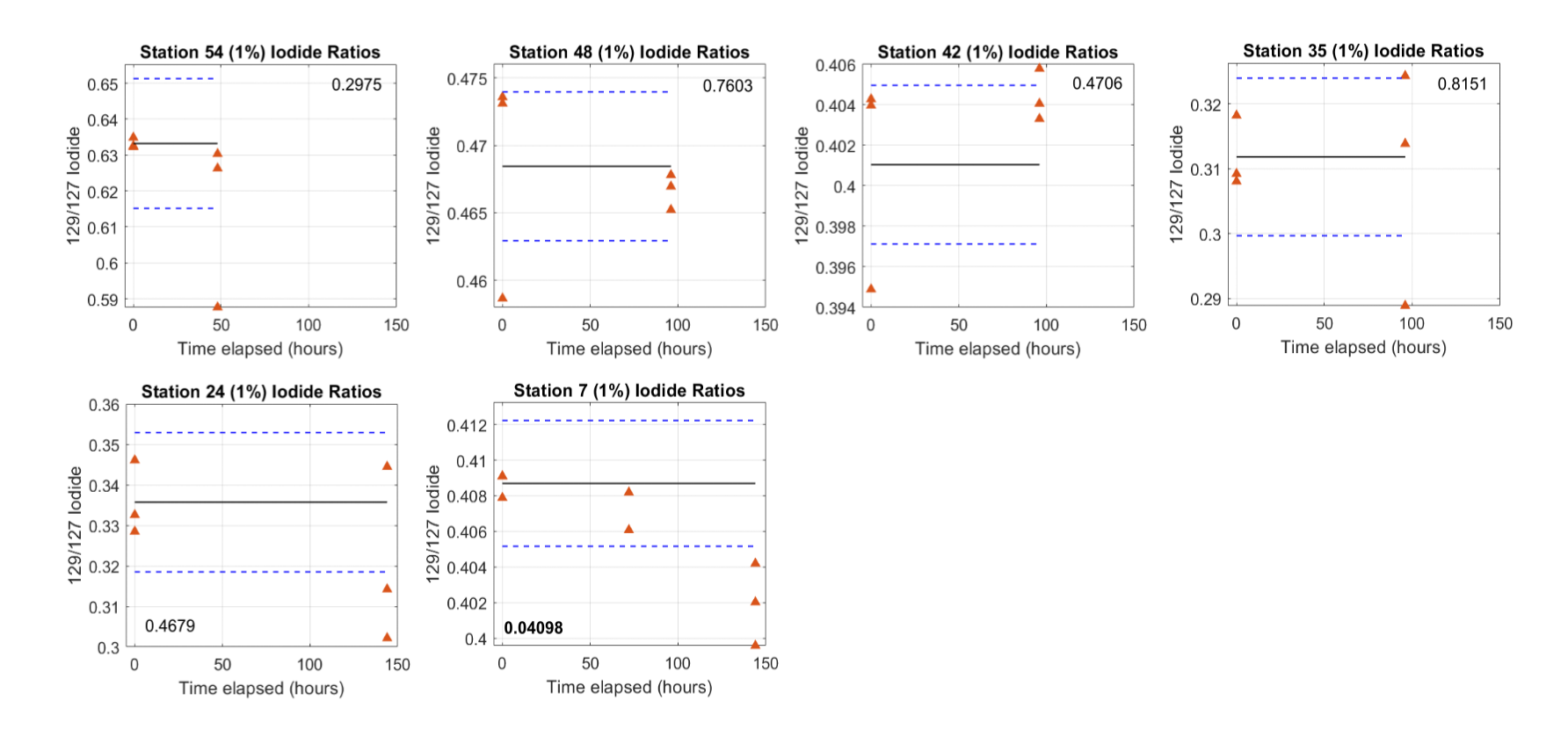


Figure 6. Plots of iodide isotope ratios from 5 stations (54, 48, 42, 35, 24, and 7) from the 1% light depth. Each plot includes every available timepoint as well as the initial average, calculated from the average of the triplicate timepoint collected at t₀ (0 hours), marked by the solid black line and one standard deviation above and below the average (dotted blue line). The value placed in the corner of each plot is the calculated p value from the performed t-tests.

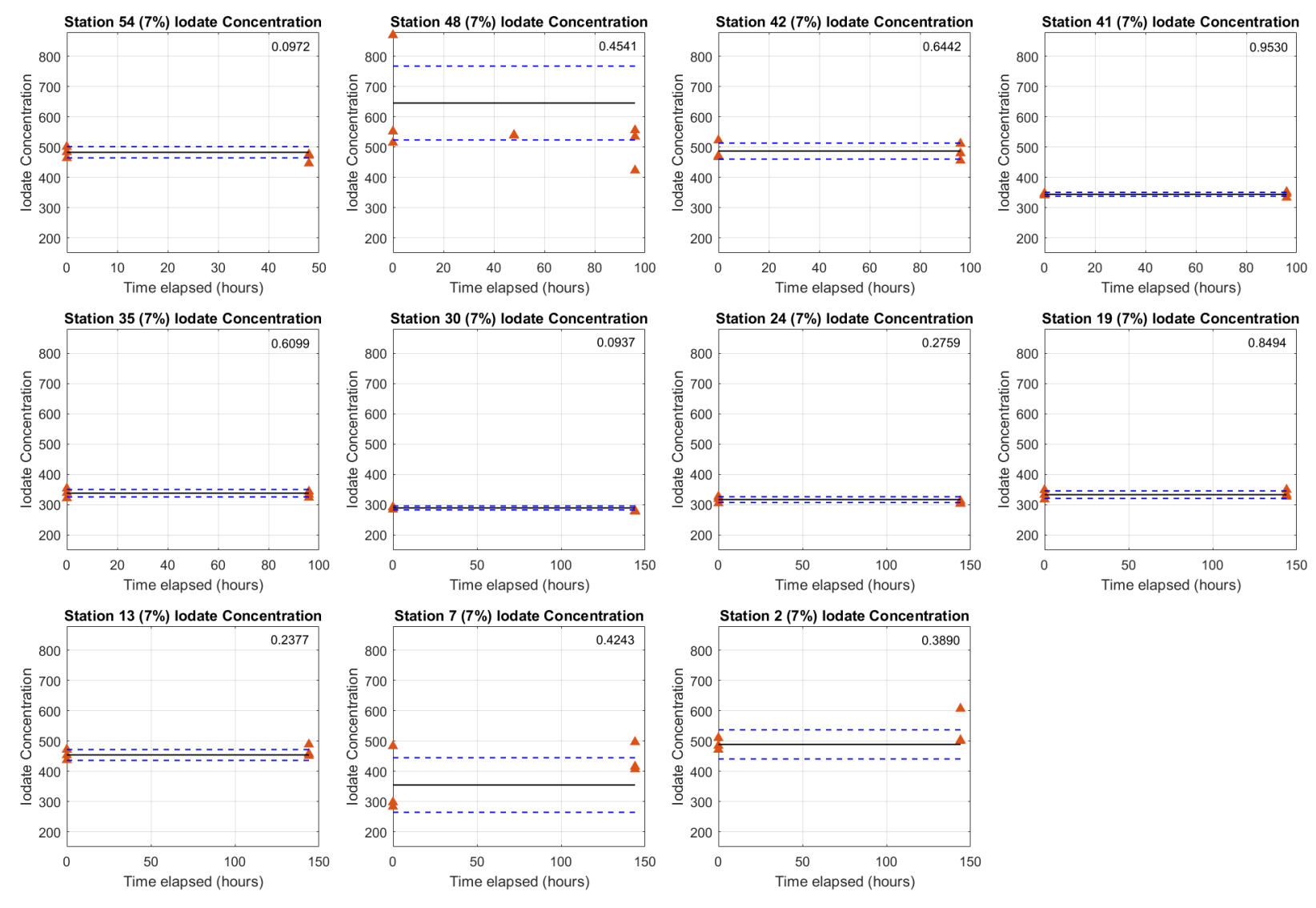


Figure 7. Plots of iodate concentrations from 11 stations (54 to 2) from the 7% light depth. Each plot includes every available timepoint as well as the initial average, calculated from the average of the triplicate timepoint collected at t₀ (0 hours), marked by the solid black line and one standard deviation above and below the average (dotted blue line). The value in the upper right corner of each plot is the calculated p value from the performed t-tests.

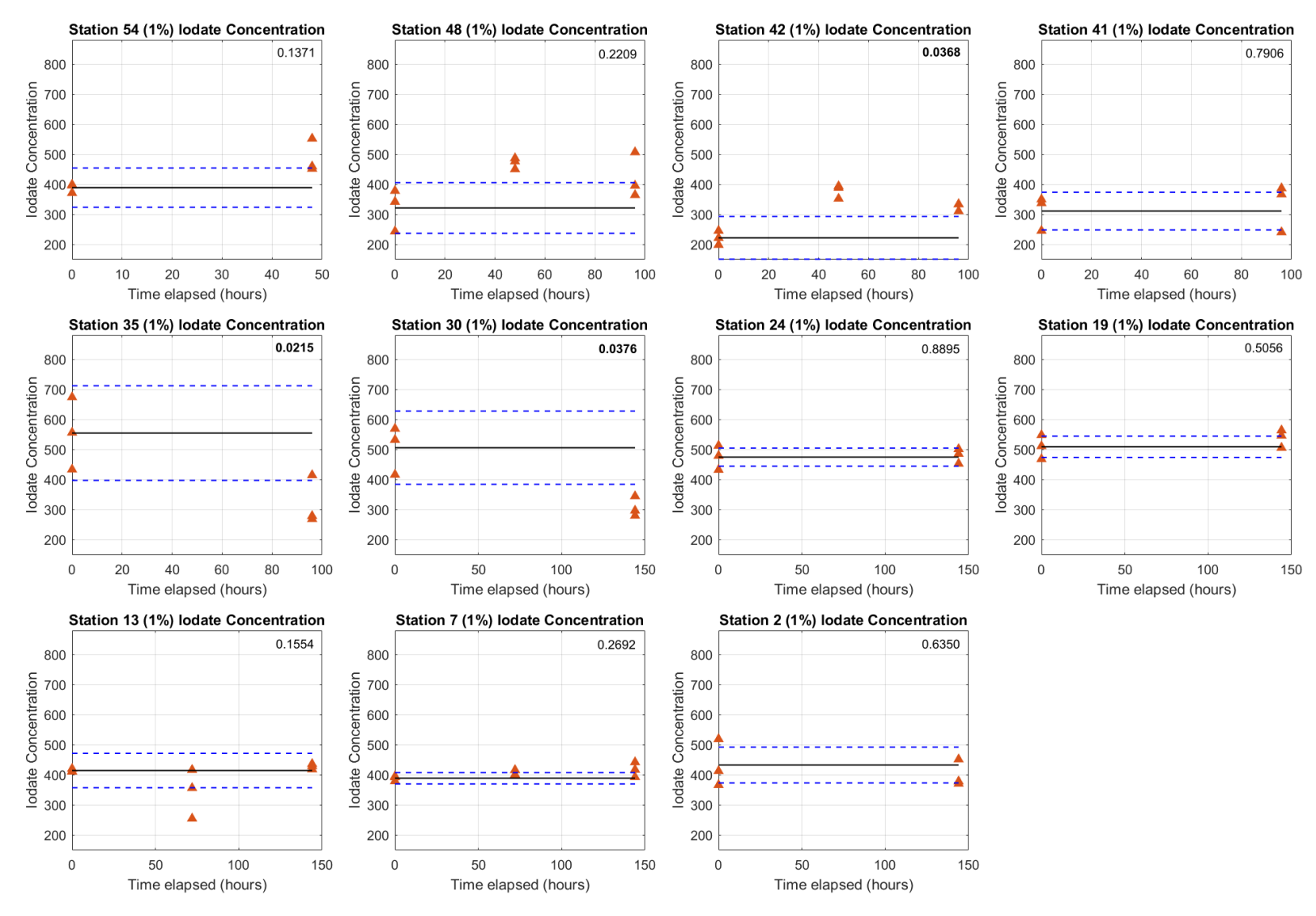


Figure 8. Plots of iodate concentrations from 11 stations (54 to 2) from the 1% light depth. Each plot includes every available timepoint as well as the initial average, calculated from the average of the triplicate timepoint collected at t_0 (0 hours), marked by the solid black line and one standard deviation above and below the average (dotted blue line). The value in the upper right corner of each plot is the calculated p value from the performed t-tests.

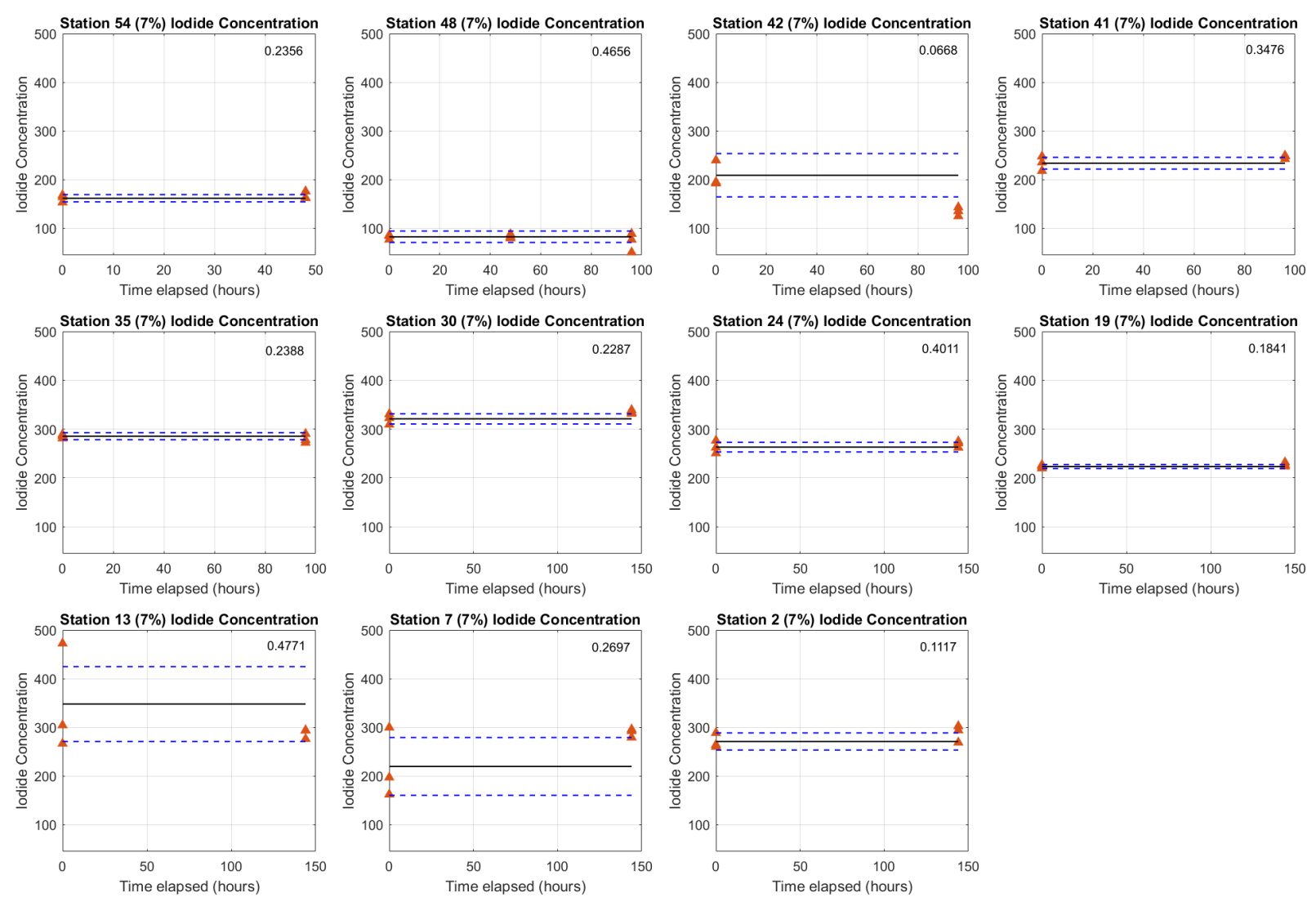


Figure 9. Plots of iodide concentrations from 11 stations (54 to 2) from the 7% light depth. Each plot includes every available timepoint as well as the initial average, calculated from the average of the triplicate timepoint collected at t_0 (0 hours), marked by the solid black line and one standard deviation above and below the average (dotted blue line). The decimal in the upper right corner of each plot is the calculated p value from the performed t-tests.

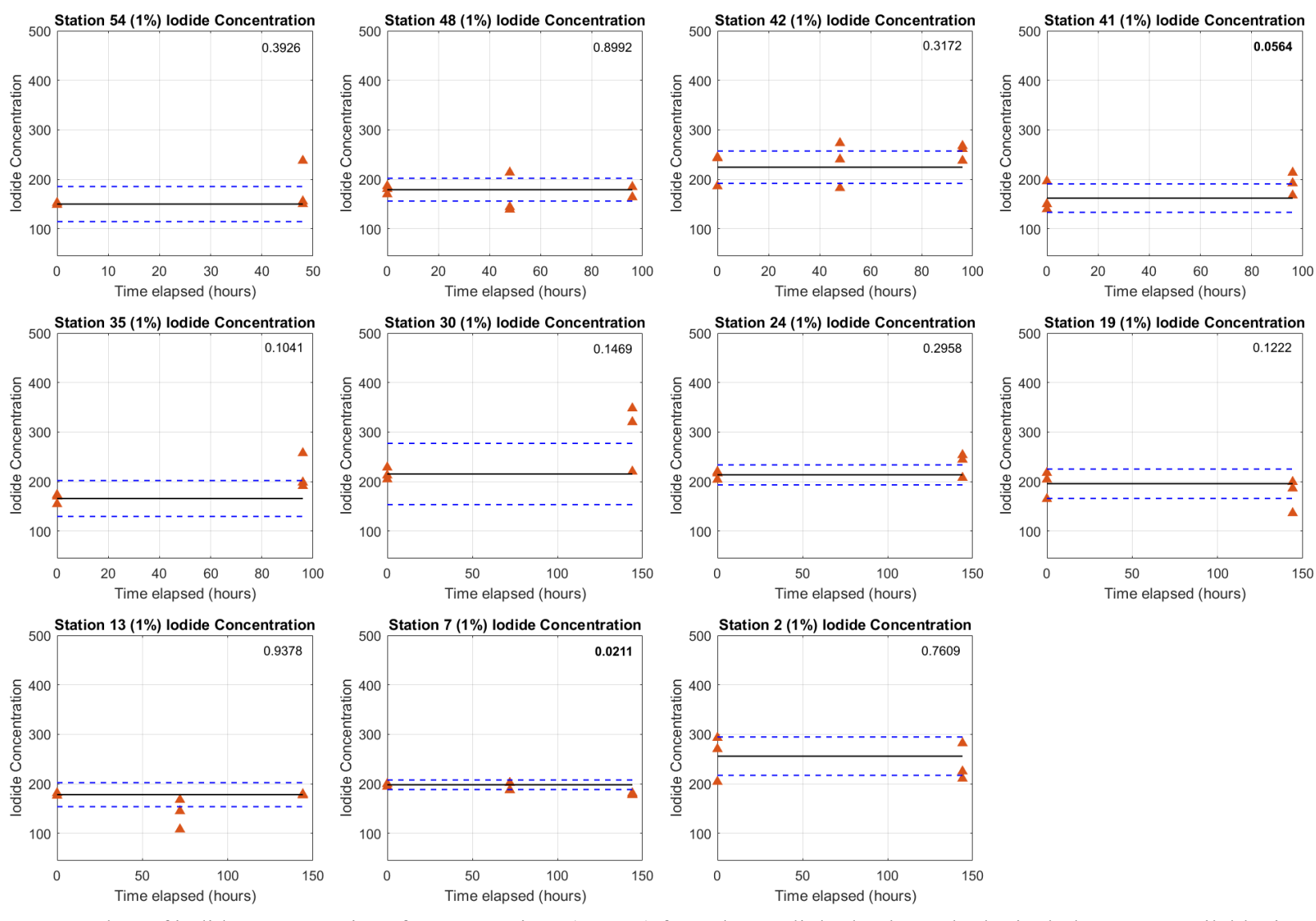


Figure 10. Plots of iodide concentrations from 11 stations (54 to 2) from the 1% light depth. Each plot includes every available timepoint as well as the initial average, calculated from the average of the triplicate timepoint collected at t_0 (0 hours), marked by the solid black line and one standard deviation above and below the average (dotted blue line). The value in the upper right corner of each plot is the calculated p value from the performed t-tests.

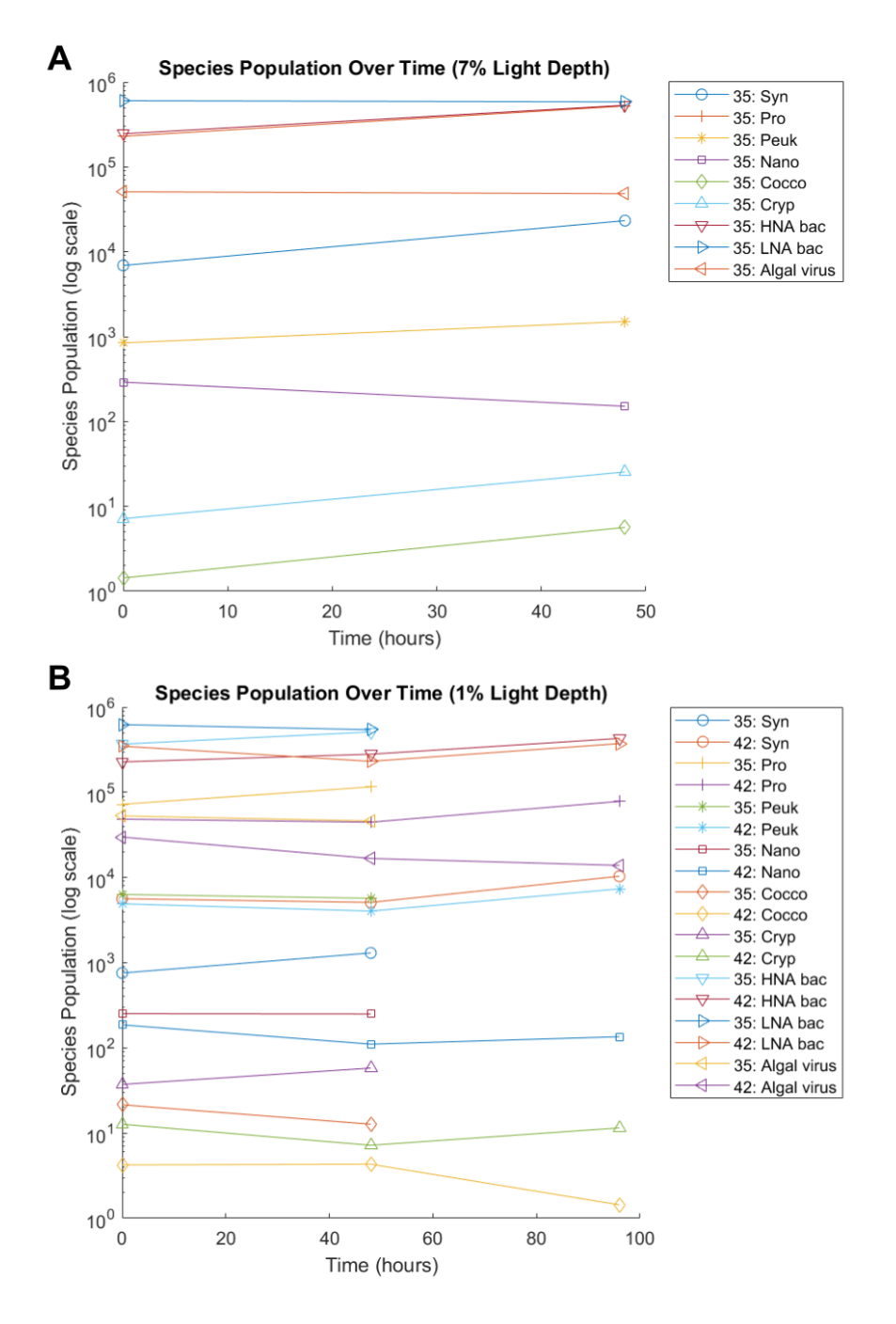


Figure 11. Plot A: taxonomic analysis of shipboard incubations over time at the 7% light percentage for station 35, which showed significant iodate isotopic changes between the initial and final timepoints. Plot B: taxonomic analysis of shipboard incubations over time at the 1% light percentage for stations 35 and 42, that showed significant isotopic changes between the initial and final timepoints. Syn is Synechococcus sp. Cyanobacteria, Pro is Prochlorococcus sp. Cyanobacteria, Peuk is Picoeukaryote phytoplankton (<2μm), Nano is Nanoeukaryote phytoplankton (approx. 2-12μm), Cocco is Coccolithophores, Cryp is Cryptophytes, HNA bac is Relatively High Nucleic Acid-containing bacteria, LNA bac is Relatively Low Nucleic Acid-containing bacteria.

DISCUSSION

The AMT-30 transect provides a unique opportunity to explore the variability and mechanisms of iodate production across different latitudinal and light regimes in the Atlantic Ocean. Our findings indicate that variability in iodine speciation and cycling is pervasive across the transect. This includes some regions with more active iodine cycling. For example, iodate production is notably enhanced at the 1% light level and at locations north of the equator sampled during boreal spring. Further, our observations highlight differences in rates and pathways of iodate production between regions. In the following sections we address these differences in pathways, the broader changes in iodine across the transect, and how this affects calculated rates of iodide oxidation.

5.1 Changes in Iodine Speciation Across the Transect

The analysis of iodine concentrations during the six-week transect of the Atlantic Meridional Transect (AMT-30) reveals significant spatial variations, both in depth and across latitude. A clear gradient in iodide concentrations was observed, with lower levels at higher latitudes (40-15° N and S) and a marked increase as the transect approached the equator. Specifically, iodide concentrations at higher latitudes were consistently at least 25% lower compared to those observed near the equator. Iodide concentrations also decreased with depth, ranging from 100 nM at the surface to approximately <10 nM at depths below 500 meters, which is consistent with the findings of Bluhm et al. (2010), who observed similar depth profiles in the Atlantic. The accumulation of iodate in deeper waters reflects its greater overall stability compared to iodide and underscores the influence of physical processes on iodine speciation (Wong et al., 2002).

Truesdale et al., (2000) measured surface iodate concentrations from the AMT. They revealed a similar pattern in iodate concentration to what is seen in previous studies with latitude: elevated iodate at high latitudes and lower values at low latitudes. The initial iodate concentrations from our incubations at the 7% and 1% light levels reveal this same pattern (Figures 7 and 8). Our measured latitudinal iodide distribution pattern is antithetical to the iodate pattern, which is consistent with other studies. Notably, however, the iodate concentrations from our depth profiles show much more variability and do not match this pattern. This is likely due to methodological differences. The iodate concentrations from incubations were measured via column

chromatography and ICPMS while the iodate from depth profiles were measured via spectrophotometry. The spectrophotometric method is known to have interferences, which can maintain precision but offset accuracy (e.g., Jones et al., 2023). Notably, the iodate concentration measurement via column chromatography and ICPMS can also have low yields (Hou et al., 2009; Wong & Brewer, 1977), which likely accounts for the lower precision in our triplicate time points from the incubations. For these reasons, we suggest that, until further investigation, iodate variations in the depth profiles measured via spectrophotometry may represent an analytical artefact.

Alternatively, differences in iodate concentrations may be attributed to the time frames of each study. The AMT-30 collected data from February 2023 through March 2023 while the data examined in Truesdale 2000 was collected between September and October of 1996 (AMT-3) and April through May of 1997 (AMT-4). This shift in time frames could account for seasonal changes in the availability of nutrients at locations along the transect, seasonality changes impacting bioactivity in the observed regions, or physical dynamics such as vertical diffusion and stratification effects (Truesdale et al., 2000).

The transect passed by and edged along the oxygen-deficient zone (ODZ) off the coast of Africa (Figure 2). However, despite the proximity to the ODZ, the data indicate no clear trend of iodate reduction to iodide in this region. Therefore, while ODZ's are known locations of high iodide (Hardisty et al., 2021; Luther, 2023; Moriyasu et al., 2020), the ODZ does not play a meaningful role in the processes examined in this study.

The deep chlorophyll maximum (DCM), a key feature in marine ecosystems, was tracked along the transect using fluorescence as a proxy, as fluorescence is strongly correlated with high phytoplankton concentrations and elevated primary productivity in surface waters. The DCM typically occurs at depths where light availability begins to decrease but nutrient concentrations remain sufficient to sustain phytoplankton growth (usually at 1-3% light percentage), resulting in a peak in chlorophyll concentrations (Moriyasu et al., 2023). This zone of heightened primary productivity plays a critical role in biogeochemical cycles, including the marine iodine cycle. Phytoplankton activity within the DCM has been shown to influence iodine speciation, particularly through enhanced reduction of iodate to iodide (Truesdale et al., 2000), which directly affects the spatial distribution of iodine species.

As the transect approached the equator, areas of high iodide concentrations were found to correlate with regions of elevated temperature and were positioned just above the DCM. This observation aligns with findings by Truesdale et al. (2000), who reported similar relationships between iodide concentrations and the DCM in the Atlantic. Further supporting this, studies in other parts of the Atlantic have demonstrated that areas with higher chlorophyll concentrations are typically associated with higher iodide levels and more active iodate oxidation (Moriyasu et al., 2023). This relationship between fluorescence, chlorophyll, and iodide concentration becomes particularly pronounced at light levels around 1%, where the iodine cycle appears more dynamic due to elevated biological activity and chlorophyll presence.

Tracking the DCM along the transect provided a valuable indicator of primary productivity and allowed for better understanding of iodine speciation patterns in the Atlantic Ocean. The correlation between DCM features, such as high fluorescence and chlorophyll concentrations, and the distribution of iodine species suggests that the biological processes within the DCM significantly impact the cycling of iodine. This reflects the broader influence of biological productivity on marine iodine cycling, highlighting the importance of the DCM as a zone where the iodine cycle is actively shaped by biotic factors. Hughes et al. (2021) demonstrated in lab cultures that ammonia oxidation, which is typically near or coincident with the DCM, can play a significant role in the iodine cycle. Their experimental work showed that ammonia-oxidizing microorganisms can oxidize iodide to iodate under controlled conditions. This finding highlights a direct biochemical pathway for iodine transformations in the presence of ammonia oxidation, suggesting that microbial activity influences iodine speciation at deeper light levels. Our shipboard incubations at the DCM provide a test to this hypothesis under ambient conditions.

These observations underscore the complex interplay of physical, chemical, and biological processes that govern iodine cycling in the upper ocean. The variability in iodate and iodide distributions, particularly within the dynamic 1% light level, highlights the intricate mechanisms at work in different marine environments. Understanding these patterns is essential for unraveling the broader implications of iodine's role in ocean biogeochemistry.

5.2 Iodate formation pathways in shipboard incubations

In analyzing the changes in iodate isotope ratios across the Atlantic transect during AMT-30, we categorized the observed patterns into three distinct groups based on the results of t-tests

conducted between the initial and final timepoints. To determine statistical significance, we employed a t-test with a threshold p-value of 0.05, where changes were considered statistically insignificant if the p-value exceeded 0.05, and significant if the p-value was below this threshold. Category 1 includes stations where no discernible change in iodate ratios were detected between the initial and final timepoints. This observation aligns with findings from Schnur et al. (2024), who reported similar stability in iodate ¹²⁹I/¹²⁷I. In our study, stations 2-30 and 54 at the 1% light level (Figure 4) and stations 2-30 and 41-54 at the 7% light level (Figure 3) displayed no significant differences, suggesting consistent conditions in these regions. Category 2 consists of stations that exhibited a significant positive shift in iodate isotope ratios. Our results show a notable increase at station 35 at the 7% light level (Figure 3). These results are similar to findings from Hardisty et al. (2020), who also observed a positive shift in iodate isotope ratios in their comparable study. Category 3 captures stations where a significant negative shift in iodate isotope ratios was observed. In our study, stations 35, 41, 42, and 48 at the 1% light level (Figure 4) showed a decrease in iodate isotope ratios between the initial and final timepoints. These findings are comparable to those reported by Streangă et al. (2023), who also identified negative shifts in iodate isotope ratios in an incubation of surface water in their work. Overall, the most dynamic changes in iodate isotope ratios during AMT-30 were observed at the 1% light level, particularly in the northern portion of the transect, encompassing stations 35-48.

The majority of our locations fall within Category 1, with a lack of significant changes in iodate isotope ratios over time at various light levels and stations. A similar finding was observed from similar iodine-129 tracer incubations from (Schnur et al., 2024). In their examination of iodine speciation and isotope ratio changes in incubations from two depths in the Sargasso Sea, Schnur and others (2024) reported no significant variation in [IO₃-] and [I⁻] concentrations and their isotope ratios over time. This finding is consistent with slow oxidation rates and other studies providing evidence that iodine redox species in surface waters tend to remain stable, at least over short time periods (Hou et al., 2001). This stability is evident in our data, particularly at stations 2-30 and 54 (Figure 3) and stations 2-30 and 41-54 (Figure 4), where iodate isotope ratios at both the 7% and 1% light levels show no significant change. An example from our data that illustrates this stability can be seen at Station 2 (Figure 3). At the 7% light level, the initial timepoint average for the three samples was 0.0069±0.00029, which only slightly increased to 0.0081±0.00068 at the final timepoint. The t-test value of 0.23 further supports the conclusion that this change is not

statistically significant. Similarly, at the 1% light level from this same station, the initial timepoint average of 0.0065 ± 0.00035 increased to 0.0071 ± 0.000423 , with a t-test value of 0.17, again indicating no significant change.

We cannot rule out that iodine cycling is active at these sites, but beyond the temporal, spatial, or analytical resolution of our experiments. Specifically, the lack of significant changes in isotope ratios in incubations from these stations may indicate that the iodine cycling is temporally punctuated (e.g., seasonal) during periods not sampled here. Alternatively, other euphotic depths not evaluated here could be important loci of iodine redox reactions. The importance of specific depths and associated conditions is evident from our comparison of 7% and 1% light levels. Lastly, iodate production may be occurring, but at rates slower than the resolution of our tracer approach. This possibility and our upper constraints on rates are discussed in detail in the next section. Regardless, however, slow or temporally isolated iodate production in the majority of our studied sites and depths is consistent with local and regional mixing processes playing an important role in regulating local iodine speciation (Chance et al., 2010; Luther, 2023; Moriyasu et al., 2020; Truesdale et al., 2000; Wadley et al., 2020).

For Category 2, the observed positive shift in iodate isotope ratios—particularly at Station 35 (Figure 3)—specifically implies a role of iodide in the production of iodate. This shift is consistent with trends reported by Hardisty et al. (2020), where similar positive changes in iodate isotope ratios were interpreted as indicative of enhanced oxidative processes. Specifically, at the 7% light level, the average iodate 129I/127I ratio increased from 0.014±0.00059 at the initial timepoint to 0.016±0.00041 at the final timepoint, with a t-test value of 0.017 supporting the statistical significance of this shift. Since iodide is the iodine species from which the tracer is mostly composed of, such a change implies a net oxidation of iodide to iodate, potentially driven by biological or photochemical processes. This same observation was made from unfiltered incubations from surface seawater from Martha's Vineyard Sound (Hardisty et al., 2020). Importantly, that study and the North Pacific study (Streangă et al., 2023) combined the iodate fraction with another fraction which has been interpreted in other studies as hosting dissolved organic iodine (Hughes et al., 2021), which provides some ambiguity as to whether iodate or iodine intermediate formation contributed to changes in iodine isotope ratios in those studies. In our study, we isolated these 2 fractions and focused on the iodate fraction specifically in order to avoid ambiguity regarding the formation of iodate from iodide. As such, our observation of increased

iodate ¹²⁹I/¹²⁷I ratios provides strong, and among the first, direct observations of iodate production from iodide in a normal marine setting.

At this same location (Station 35 at 7%) the iodide ¹²⁹I/¹²⁷I decrease between the average initial (0.31±0.00011) and average final (0.31±0.00016) timepoints with a calculated p-value of 0.010. This change in iodide (difference in iodide: 0.0017) is notable but less distinct compared to the iodate ¹²⁹I/¹²⁷I ratios (difference in iodate: 0.0020) from this same station and light depth. Together, these suggests that iodate reduction and formation were occurring simultaneously.

Another observed increasing trend in the iodate $^{129}\text{I}/^{127}\text{I}$ between the initial and final timepoints is Station 7 at the 1% light level. Although the p-value for the performed t-test is 0.06 which is just on the cusp of statistical significance (p \leq 0.05). At Station 7, sampled at the 1% light level, the iodate isotope ratio ($^{129}\text{I}/^{127}\text{I}$) exhibited a notable change over time first decreasing then increasing overall. The initial decrease in the ratio between t_0 and t_1 was not statistically significant (p = 0.12). However, the comparison between the middle and final timepoints (t_1 and t_f) yielded a p-value of 0.034, indicating a statistically significant increase. This suggests a potential conversion of iodide to iodate. Conversely, the iodide $^{129}\text{I}/^{127}\text{I}$ ratio decreased, with a p-value of 0.041 indicating a statistically significant decrease over the course of the incubation. The observed decrease followed by an increase in iodate isotope ratios at Station 7 (1%) suggests dynamic iodate formation pathways, with intermediates potentially playing a significant role before complete conversion. Similar inferences were made by \$treangă et al. (2023) based on internal changes in iodate isotope ratios in unfiltered incubations. Additionally, the decrease in iodide isotope ratios points to potential iodate reduction and iodide oxidation during the experiment.

The final observed pattern from our data, Category 3, reveals a significant negative shift in iodate isotope ratios over time in 4 out of 22 of the stations/depth evaluated here. The same observation was made in Ştreangă et al. (2023) in their iodine-129 tracer incubation from North Pacific surface water. Our study identified a marked decline in iodate isotope ratios at Stations 35, 41, 42, and 48, all at the 1% light level, (Figure 5). For example, at Station 42, the iodate ¹²⁹I/¹²⁷I ratio decreased from an average of 0.016±0.00037 at the initial timepoint to 0.0079±0.00070 at the final timepoint, with a t-test value of 0.0011 indicating a statistically significant change. Importantly, at Station 42 (1% light level) a statistically significant increase in the iodate concentrations was also observed, providing additional evidence of iodate production (Figure 4).

Importantly, a decrease in the iodate isotope ratio requires iodate formation rates to be highest from a source other than the iodide-129 tracer (i.e., a source dominated by iodine-127). This implies a likely role of iodine intermediates in the formation of iodate. It is possible that iodide is part of the pathway, but that the rates of iodide oxidation to the required intermediates are slower than the subsequent oxidation of intermediates to iodate, thus diluting any isotopic signal from iodide. Our study did not include controls to isolate specific reaction mechanisms or pathways, but the study of Streangă et al. (2023) —which made a similar observation—did include controls. Specifically, Ştreangă et al. (2023) observed a lack of significant changes in iodate isotope ratios in filtered controls, pointing to the possibility that microorganisms excluded during filtering (0.2 µm) catalyzed the reaction. Further, thermodynamic calculations provide evidence that iodine intermediates are required for iodate formation (Luther, 2023). Specifically, Luther (2023) demonstrated that the formation of iodate from iodide involves a complex multi-step process that includes the oxidation of iodide (I⁻) to hypoiodous acid (HOI), followed by the disproportionation of HOI to produce diatomic iodine (I₂) and further oxidation steps leading to the final formation of iodate (IO₃⁻). Each of these intermediate steps involves specific reaction conditions and equilibria that can shift depending on the surrounding chemical environment, such as pH, the presence of catalysts, or microbial activity (Luther, 2023). The involvement of these intermediates is crucial, as they dictate the overall kinetics of the process and ultimately control the isotopic composition of the iodate formed. This aligns with our observations and those of Ștreangă et al. (2023), indicating that iodate production may be largely governed by the dynamics of these intermediate species rather than by the initial oxidation of iodide.

5.3 Rates calculations

Understanding the rates at which iodate, iodide, and potential intermediates undergo transformations in the ocean is crucial for elucidating the dynamics of the marine iodine cycle. These rates provide insights into the underlying pathways and mechanisms driving the observed changes in iodate concentrations and ratios over time. This section explores the variability in these rates across different stations and light levels, highlighting the same 3 categories from the previous section: no discernible change in iodate isotope ratios (Scenario 1), a positive shift in iodate isotope ratios (Scenario 2), and a negative shift in iodate isotope ratios (Scenario 3). By examining the calculated rates in conjunction with potential physical, chemical, and biological mechanisms, we

aim to shed light on the processes governing iodine speciation in the marine environment. The following analysis is summarized in Tables 4 and 5, as well as Figure 12, and is supported by comparisons with previous studies to contextualize these findings within the broader framework of marine biogeochemistry.

Rate calculations of iodate formation were performed for each incubation at 1% and 7% light according to previous approaches (Hardisty et al., 2020; Schnur et al., 2024; Ştreangă et al., 2023). For these calculations, we modeled changes in iodate concentration based on the measured ¹²⁹I/¹²⁷I of iodate. These calculations all start with the average measured iodate concentration at t₀ as the initial timepoint. We then calculated the ¹²⁹IO₃- and ¹²⁷IO₃- concentrations at t₀ for each of the triplicates using measured ¹²⁹I/¹²⁷I of iodate at t₀. Next, we solved for the ¹²⁹IO₃- and ¹²⁷IO₃- additions required to achieve the measured isotope ratio of subsequent time points, which are summed to determine total IO₃- for these time points. Importantly, specific considerations were made regarding the isotopic composition of the iodate precursor for each of the generalized three scenarios that we observed. These are outlined in more detail below. Lastly, in each case, rates were calculated according to zeroeth, first, and second order (Hardisty et al., 2020; Schnur et al., 2024; Ştreangă et al., 2023). These were each considered because there is uncertainty regarding the specific reaction mechanism and associated reaction order, but also in an attempt to constrain the reaction order using our experiments.

For Scenario 1, where no change in iodate ¹²⁹I/¹²⁷I ratios was observed, we constrain the maximum rates possible in which the final time points remain within 1 standard deviation of our initial time points—thus within the uncertainty of our data (e.g., Schnur et al., 2024). These values are shown in Tables 4 and 5, where they are within brackets to denote that they represent maximum constraints. Importantly, we considered the maximum iodate production rates associated with a positive shift in iodate isotope ratios (implying iodate formation from an iodide source matching the ¹²⁹I/¹²⁷I measured at t₀) as well as the maximum rates associated with a negative shift in iodate isotope ratios (implying a non-specific ¹²⁷I-only sources to iodate). Notably, given the initially low ¹²⁹I/¹²⁷I of iodate, the iodate isotopic changes are more sensitive to additions with the isotopic composition of our measured ¹²⁹I/¹²⁷I of iodide, and thus the calculated maximum rates are much lower in this scenario relative to iodine-127 only additions.

In scenarios where no significant change in iodate isotope ratios is observed, as seen in the majority of our experiments, the first order rates calculated range from 9 to 37 yr⁻¹ for the ¹²⁷I⁻

addition at the 7% light level (Table 4) and from 4 to 33 yr⁻¹ for the ¹²⁷I⁻ addition at the 1% light level (Table 5). The ¹²⁹I⁻ additions for the 7% light level (Table 4) for the first order rates range from 0.156 to 6.94 yr⁻¹ and for the 1% light level the rates range from 2.25 to 3.16 yr⁻¹. The lack of significant change in iodate isotope ratios indicates that the iodine cycle at these locations is not driven primarily by chemical or biological transformations but rather by physical mixing and advection. The role of physical mixing in controlling iodate levels has been supported by previous studies, which have shown that in regions with strong water column mixing, the distribution of iodine species is often uniform, leading to minimal changes in iodate isotope ratios (Truesdale et al., 2000; Wong & Brewer, 1977). These slow iodine redox transformations also align with the findings of Schnur et al. (2024), who also inferred from similar experimental observations that physical processes dominate in Atlantic surface waters near Bermuda.

Scenario 2 only applies to station 35 at the 7% light level, where a positive shift in iodate isotope ratios is observed. This observation specifically implies iodate formation from iodide, so the rate calculation was only performed for an increase in ¹²⁹I/¹²⁷I of iodate sourced from the measured ¹²⁹I/¹²⁷I of iodide. We do recognize that ¹²⁷I-only sources to iodate could occur alongside iodide oxidation to iodate, as we suggest for station 7 (1%), but to maintain simplicity and in the absence of direct constraints we ignore this possibility. The zeroth-order rate calculated at station 35 is approximately 1321 nM/yr, which is about ten times as fast as the zeroth-order reaction rates reported by Hardisty et al. (2020), who also documented an increase in iodate isotope ratios in similar experiments, but at rates between 118 and 189 nM/yr. This substantial difference in rates between the 2 studies suggests more active biogeochemical processes such as microbial oxidation of iodide, which can be influenced by environmental factors like light availability, organic matter concentration, and the presence of reactive oxygen species (Campos et al., 1996; Hardisty et al., 2020). Regardless, our survey results and comparison to other studies (Hardisty et al., 2020; Schnur et al., 2024; Ştreangă et al., 2023) clearly suggest that iodate formation from iodide is not widespread, but when active there is potential for large variations in reaction rates.

For Scenario 3, where negative shift in iodate isotope ratios is observed, our rate calculations exclusively consider an unspecified ¹²⁷I source for iodate formation. Analogous to Scenario 2, we recognize that oxidation of the radiolabeled iodide could occur simultaneously with radio-iodine free sources, but to maintain simplicity and in the absence of direct constraints we ignore this possibility. At the relevant stations—i.e., stations 35, 41, 42, and 48 at the 1% light

level—the rates of iodate formation are notably high, ranging from 51,112 to 142,944 nM/yr for zeroeth order and 92 to 126 yr⁻¹ for first order rates (Table 5 and Figure 12). These rapid rates suggest that the iodate production is occurring at an accelerated pace, possibly due to a multi-step reaction mechanism involving iodine intermediates. Comparison of reaction order fit to the calculated iodate concentrations suggests that first-order reactions may be most applicable for this scenario (Figure 12). This supports the idea that the process involves complex biochemical pathways (Luther, 2023). This dynamic cycling likely involves the transient accumulation of iodine intermediates, which then rapidly convert back to iodate, resulting in the observed negative shift. Ştreangă et al. (2023) reported similar findings, reporting a first order reaction rate of 157 yr⁻¹ which overlaps with the range observed here.

The predicted iodate production rates for stations with decreased iodate isotope ratios are notably higher than any observed changes in iodate concentrations (Figures 3 and 4). For example, at stations 35 through 48 at the 1% light level, the predicted rates of iodate production (as shown in Figure 12 and Table 5) are much higher than the measured iodate concentrations at the final timepoints (Figure 5). When rates far exceed what is directly observed, this indicates a pattern of extensive recycling of iodine between endmember and intermediate pools. This disparity suggests that our calculations constrain a gross rate of iodate formation and that the net rate is offset by back reactions from iodate to iodine intermediates that also occur at a significant rate. Given these observations, we suggest that the isotopic trend and reaction order fit could indicate that isotopic equilibrium between the intermediate pools and the iodate pool is being established during rapid exchange. Thus, changes in ¹²⁹I/¹²⁷I of iodate decelerate at the final stages of the incubation as the two isotopic pools become more similar. If so, the rates could be even faster than that calculated here, since we assumed an iodate source that was exclusively ¹²⁷I. Further, given the relatively large concentration of iodine-127 additions required to detect changes in the ¹²⁹I/¹²⁷I of iodate, we suggest similar reactions are perhaps widespread but might be more easily detected in tracer experiments with the ¹²⁹I added directly as iodate. Regardless, the observed trend for Scenario 3 is still not universal; most stations and depths show no change in either concentration or isotope ratios between incubation timepoints. This comparison to other stations provides confidence that the observed phenomenon of accelerated iodate exchange with intermediates is localized, potentially limited to stations 35 through 48 at the 1% light level.

Table 4. Table of calculated iodide oxidation rates for stations at the 7% light level, in nM/year⁻¹. Values are the rates, dashes are where a rate was not calculated due to an observed statistically significant change between timepoints in the other category, and "NC" is where a calculation was unable to be performed due to missing variables. Brackets indicate values calculated using the upper standard deviation value for the highest rate possible.

Rates at the 7% Light

Percentage						
Site	Zero Order I-	Zero Order I-	First Order I-	First Order I-	Second Order I-	Second Order I-
Number	127 (nM/yr)	129 (nM/yr)	127 (yr ⁻¹)	129 (yr ⁻¹)	127 (nM ⁻¹ yr ⁻¹)	129 (nM ⁻¹ yr ⁻¹)
2	[4.77E+03]	[7.67E+01]	[9.05E+00]	[1.56E-01]	[1.72E-02]	[3.16E-04]
7	[5.58E+03]	[1.32E+02]	[1.40E+01]	[3.69E-01]	[3.53E-02]	[1.03E-03]
13	[4.53E+03]	[9.82E+01]	[9.25]	[2.14E-01]	[1.89E-02]	[4.68E-04]
19	[5.15E+03]	NC	[1.38E+01]	NC	[3.70E-02]	NC
24	[5.18E+03]	NC	[1.45E+01]	NC	[4.07E-02]	NC
30	[3.51E+03]	NC	[1.11E+01]	NC	[3.50E-02]	NC
35	-	1.32E+03	-	3.83	-	1.11E-02
41	[6.49E+03]	NC	[1.72E+01]	NC	[4.55E-02]	NC
42	[1.65E+04]	[3.74E+03]	[2.88E+01]	[6.94]	[5.08E-02]	[1.29E-02]
48	[6.46E+03]	[1.12E+03]	[9.49]	[1.62]	[1.40E-02]	[2.34E-03]
54	[2.00E+04]	[2.35E+02]	[3.73E+01]	[4.83E-01]	[6.99E-02]	[9.90E-04]

Table 5. Table of calculated iodide oxidation rates for stations at the 1% light level, in nM/year⁻¹. Values are the rates, dashes are where a rate was not calculated due to an observed statistically significant change between timepoints in the other category, and "NC" is where a calculation was unable to be performed due to missing variables. Brackets indicate values calculated using the upper standard deviation value for the highest rate possible.

Rates at the 1% Light

Percentage

Site Number	Zero Order I- 127 (nM/yr)	Zero Order I- 129 (nM/yr)	First Order I ⁻ 127 (yr ⁻¹)	First Order I- 129 (yr ⁻¹)	Second Order I- 127 (nM ⁻¹ yr ⁻¹)	Second Order I- 129 (nM ⁻¹ yr ⁻¹)
2	[5.56E+03]	NC	[1.17E+01]	NC	[2.45E-02]	NC
7	[1.58E+04]	[1.72E+03]	[3.37E+01]	[3.16]	[7.28E-02]	[5.90E-03]
13	[7.32E+03]	NC	[1.55E+01]	NC	[3.30E-02]	NC
19	[8.07E+03]	[1.21E+03]	[1.41E+01]	[2.25]	[2.47E-02]	[4.20E-03]
24	[6.47E+03]	[1.21E+03]	[1.23E+01]	[2.40]	[2.34E-02]	NC
30	[2.25E+03]	NC	[4.29]	NC	[8.18E-03]	NC
35	1.43E+05	-	1.21E+02	-	1.21E-01	-
41	5.11E+04	-	9.23E+01	-	1.85E-01	-
42	6.08E+04	-	1.26E+02	-	3.07E-01	-
48	6.59E+04	-	1.03E+02	-	1.88E-01	-
54	[2.66E+04]	-	[5.68E+01]	-	[1.23E-01]	-

5.5 Implications

Observations of iodate production have remained elusive, but this study demonstrates that iodine cycling processes are actively occurring in the ocean, with both iodine oxidation and reduction contributing to the observed variability. Understanding these mechanisms is essential for accurately modeling cycling in the ocean and its interactions with other elements (Wadley et al., 2020; Lu et al., 2018; Cheng et al., 2024), such as carbon and nitrogen, as well as predicting how marine biogeochemical cycles might respond to environmental changes like ocean acidification or warming. For example, while global-scale modeling approaches assuming generalized reaction rates for iodide oxidation to iodate may be applicable (e.g., Cheng et al., 2024), ours and the combination of other recent tracer studies demonstrate a diversity of rates from location to location. That said, the challenge remains of determining the natural mechanisms and required conditions for driving these rate variations, which is essential for incorporation into global iodine cycling models.

This study also sheds light on the potential pathways of iodide oxidation. The observation of enhanced iodate production at the 1% light level overlapping with the DCM provides some support for links between iodate production and ammonia oxidation (Hughes et al., 2021). While ammonia oxidation rates were not measured in this study, previous nitrogen tracer studies from the AMT transect have demonstrated that this process is most active at the DCM (Rees et al., 2015), which is generally true globally. Iodide oxidation to iodate was observed in laboratory cultures of ammonium oxidizing bacteria while our data reinforce this connection in the natural environment. Importantly, however, our results from the DCM do not clearly link iodate production to iodide oxidation, instead suggesting an important role for intermediates, including oxidation and reduction. Future work should consider more directly linking iodate production and ammonia oxidation. For example, this could include controls limiting ammonia oxidation in shipboard experiments similar to that here where iodate production is being traced. Similarly, tracking ammonia oxidation rates and iodate production rates in the same experiments could provide evidence of coupled increases and decreases in rates, thus linking the processes.

This research has profound implications for paleoceanography, particularly in the context of redox proxies, as iodine is increasingly used to infer past redox conditions and the oxygenation state of ancient waters. The study's findings on iodate production and the role of intermediates offer a new framework for interpreting these proxies, as understanding the modern mechanisms of

iodate formation and variability allows for better interpretation of historical changes in iodine cycling and redox states preserved in sedimentary records. However, the rates and pathways of iodate production present significant challenges for both modern and ancient iodine cycle models (Cheng et al., 2024; Wadley et al., 2020). The observed variability in iodate production complicates the application of iodine-based proxies for quantitative interpretations of past ocean conditions. Nonetheless, the insights from this study contribute crucial data for improving these models, particularly in simulating the balance between oxidation and reduction reactions in iodine cycling. By identifying the key processes that drive iodine transformations, this research enhances our ability to reconstruct ancient ocean conditions, assess their impact on Earth's climate over geological timescales, and refine models incorporating iodine isotopes as paleo-redox indicators.

CONCLUSION

This study offers a comprehensive analysis of iodine cycling in the Atlantic Ocean, integrating field observations with a radioactive iodine-129 tracer to uncover the complexity of iodate production mechanisms. The observed iodate production occurred through multiple pathways, revealing three distinct trends: no discernible change, a positive shift, and a negative shift in iodate isotope ratios. The variability in these trends, along with quantified rates that differed by depth and location, underscores the intricate interplay between biological and physical processes in iodine cycling. Notably, recycling of intermediates plays a crucial role in these dynamics, with most locations exhibiting no significant iodate production, while northern (boreal spring) locales at 1% light showed the most activity. These findings have important implications for improving models of iodine cycling and refining the use of iodine as a paleo-redox proxy. Future research should aim to refine experimental methods and explore seasonal and regional variations to further elucidate the mechanisms governing iodine dynamics in marine environments, enhancing our understanding of both modern and historical iodine cycles.

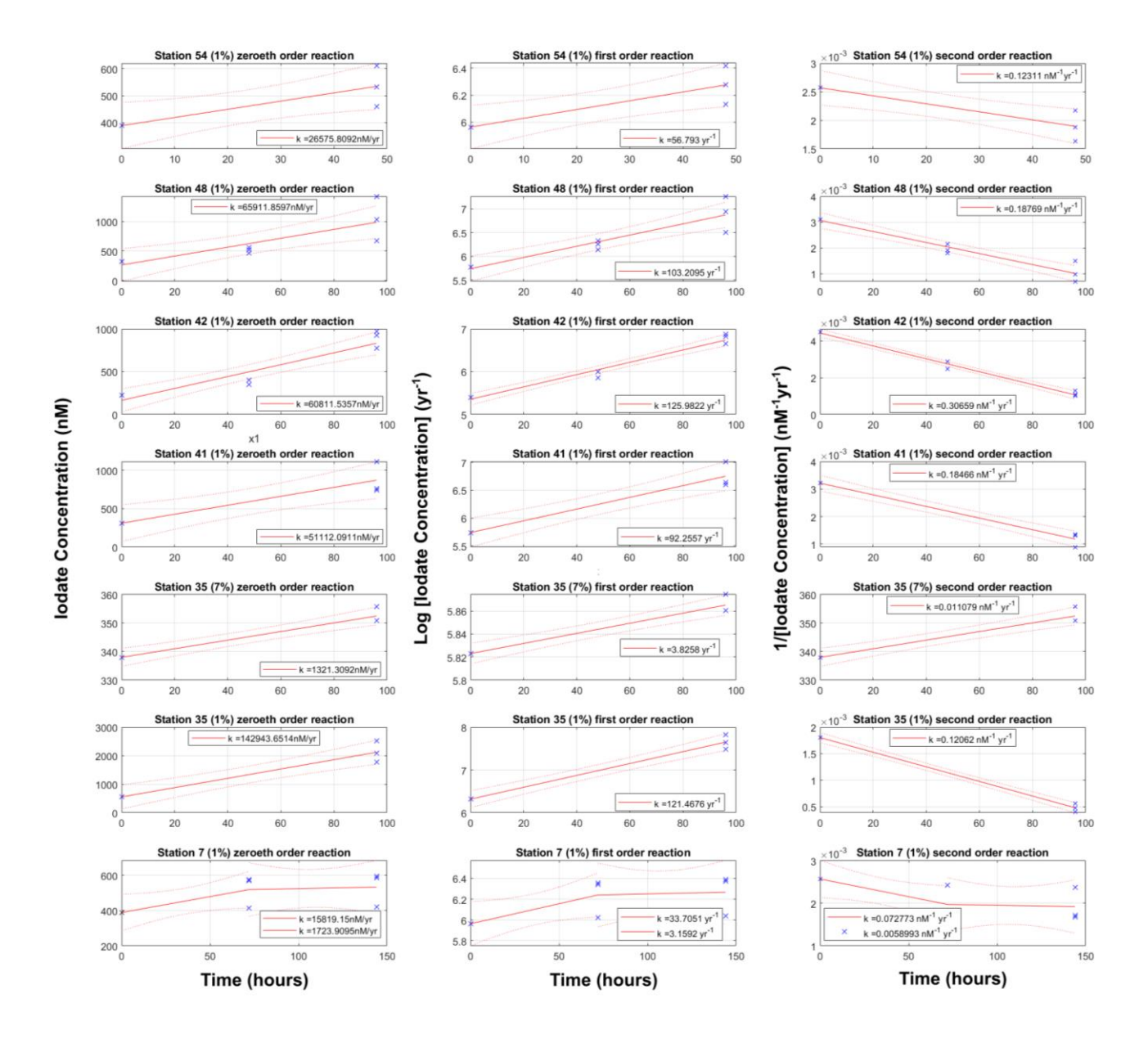


Figure 12. Plots showing each station where a statistically significant change occurred between initial and final timepoints and the associated calculated rate. Each rate includes a zeroth, first, and second order variation with a line of best fit in red for each plot and the rate value plotted as a blue "x".

BIBLIOGRAPHY

- Aiken, J., Brewin, R. J. W., Dufois, F., Polimene, L., Hardman-Mountford, N. J., Jackson, T., Loveday, B., Hoya, S. M., Dall'Olmo, G., Stephens, J., & Hirata, T. (2017). A synthesis of the environmental response of the North and South Atlantic Sub-Tropical Gyres during two decades of AMT. *Progress in Oceanography*, *158*, 236–254. https://doi.org/10.1016/J.POCEAN.2016.08.004
- Aiken, J., Pradhan, Y., Barlow, R., Lavender, S., Poulton, A., Holligan, P., & Hardman-Mountford, N. (2009). Phytoplankton pigments and functional types in the Atlantic Ocean: A decadal assessment, 1995–2005. *Deep Sea Research Part II: Topical Studies in Oceanography*, 56(15), 899–917. https://doi.org/10.1016/J.DSR2.2008.09.017
- Aiken, J., Rees, N., Hooker, S., Holligan, P., Bale, A., Robins, D., Moore, G., Harris, R., & Pilgrim, D. (2000). The Atlantic Meridional Transect: Overview and synthesis of data. *Progress in Oceanography*, 45(3–4), 257–312. https://doi.org/10.1016/S0079-6611(00)00005-7
- Bluhm, K., Croot, P., Wuttig, K., & Lochte, K. (2010). Transformation of iodate to iodide in marine phytoplankton driven by cell senescence. *Aquatic Biology*, *11*(1), 1–15. https://doi.org/10.3354/AB00284
- Campos, M. L. A. M., Farrenkopf, A. M., Jickells, T. D., & Luther, G. W. (1996). A comparison of dissolved iodine cycling at the Bermuda Atlantic Time-series Station and Hawaii Ocean Time-series Station. *Deep Sea Research Part II: Topical Studies in Oceanography*, 43(2–3), 455–466. https://doi.org/10.1016/0967-0645(95)00100-X
- Carpenter, L. J., MacDonald, S. M., Shaw, M. D., Kumar, R., Saunders, R. W., Parthipan, R., Wilson, J., & Plane, J. M. C. (2013). Atmospheric iodine levels influenced by sea surface emissions of inorganic iodine. *Nature Geoscience*, *6*(2), 108–111. https://doi.org/10.1038/NGEO1687
- Chance, R., Baker, A. R., Carpenter, L., & Jickells, T. D. (2014). The distribution of iodide at the sea surface. *Environmental Science: Processes & Impacts*, *16*(8), 1841–1859. https://doi.org/10.1039/C4EM00139G
- Chance, R., Tinel, L., Sarkar, A., Sinha, A. K., Mahajan, A. S., Chacko, R., Sabu, P., Roy, R., Jickells, T. D., Stevens, D. P., Wadley, M., & Carpenter, L. J. (2020). Surface Inorganic Iodine Speciation in the Indian and Southern Oceans From 12°N to 70°S. *Frontiers in Marine Science*, 7, 553458. https://doi.org/10.3389/FMARS.2020.00621/BIBTEX
- Chance, R., Weston, K., Baker, A. R., Hughes, C., Malin, G., Carpenter, L., Meredith, M. P., Clarke, A., Jickells, T. D., Mann, P., & Rossetti, H. (2010). Seasonal and interannual variation of dissolved iodine speciation at a coastal Antarctic site. *Marine Chemistry*, *118*(3–4), 171–181. https://doi.org/10.1016/J.MARCHEM.2009.11.009

- Cheng, K., Ridgwell, A., & Hardisty, D. S. (n.d.). *Characterizing the marine iodine cycle and its relationship to ocean deoxygenation in an Earth System model*. https://doi.org/10.5194/egusphere-2024-677
- Edwards, A., & Truesdale, V. W. (1997). Regeneration of Inorganic Iodine Species in Loch Etive, a Natural Leaky Incubator. *Estuarine, Coastal and Shelf Science*, 45(3), 357–366. https://doi.org/10.1006/ECSS.1996.0185
- Hardisty, D. S., Horner, T. J., Evans, N., Moriyasu, R., Babbin, A. R., Wankel, S. D., Moffett, J. W., & Nielsen, S. G. (2021). Limited iodate reduction in shipboard seawater incubations from the Eastern Tropical North Pacific oxygen deficient zone. *Earth and Planetary Science Letters*, 554, 116676. https://doi.org/10.1016/J.EPSL.2020.116676
- Hardisty, D. S., Horner, T. J., Wankel, S. D., Blusztajn, J., & Nielsen, S. G. (2020a). Experimental observations of marine iodide oxidation using a novel sparge-interface MC-ICP-MS technique. *Chemical Geology*, *532*, 119360. https://doi.org/10.1016/J.CHEMGEO.2019.119360
- Hardisty, D. S., Horner, T. J., Wankel, S. D., Blusztajn, J., & Nielsen, S. G. (2020b). Experimental observations of marine iodide oxidation using a novel sparge-interface MC-ICP-MS technique. *Chemical Geology*, *532*, 119360. https://doi.org/10.1016/J.CHEMGEO.2019.119360
- He, P., Hou, X., Aldahan, A., Possnert, G., & Yi, P. (2013). Iodine isotopes species fingerprinting environmental conditions in surface water along the northeastern Atlantic Ocean. *Scientific Reports 2013 3:1*, *3*(1), 1–8. https://doi.org/10.1038/srep02685
- Henson, S. A. (2014). Slow science: the value of long ocean biogeochemistry records. *Philosophical Transactions of the Royal Society A: Mathematical, Physical and Engineering Sciences*, 372(2025). https://doi.org/10.1098/RSTA.2013.0334
- Henson, S. A., Sanders, R., & Madsen, E. (2012). Global patterns in efficiency of particulate organic carbon export and transfer to the deep ocean. *Global Biogeochemical Cycles*, *26*(1). https://doi.org/10.1029/2011GB004099
- Hepach, H., Hughes, C., Hogg, K., Collings, S., & Chance, R. (2020). Senescence as the main driver of iodide release from a diverse range of marine phytoplankton. *Biogeosciences*, 17(9), 2453–2471. https://doi.org/10.5194/BG-17-2453-2020
- Hou, X., Aldahan, A., Nielsen, S. P., Possnert, G., Nies, H., & Hedfors, J. (2007). Speciation of 129I and 127I in seawater and implications for sources and transport pathways in the North Sea. *Environmental Science and Technology*, 41(17), 5993–5999. https://doi.org/10.1021/ES070575X/SUPPL_FILE/ES070575XSI20070731_030249.PDF

- Hou, X., Chen, C., Ding, W., & Chai, C. (1999). Study on chemical species of iodine in human liver. *Biological Trace Element Research*, 69(1), 69–76. https://doi.org/10.1007/BF02783916/METRICS
- Hou, X., Dahlgaard, H., & Nielsen, S. P. (2001). Chemical speciation analysis of 129I in seawater and a preliminary investigation to use it as a tracer for geochemical cycle study of stable iodine. *Marine Chemistry*, 74(2–3), 145–155. https://doi.org/10.1016/S0304-4203(01)00010-X
- Hou, X., Hansen, V., Aldahan, A., Possnert, G., Lind, O. C., & Lujaniene, G. (2009). A review on speciation of iodine-129 in the environmental and biological samples. *Analytica Chimica Acta*, 632(2), 181–196. https://doi.org/10.1016/J.ACA.2008.11.013
- Hughes, C., Barton, E., Hepach, H., Chance, R., Pickering, M. D., Hogg, K., Pommerening-Röser, A., Wadley, M. R., Stevens, D. P., & Jickells, T. D. (2021). Oxidation of iodide to iodate by cultures of marine ammonia-oxidising bacteria. *Marine Chemistry*, 234, 104000. https://doi.org/10.1016/J.MARCHEM.2021.104000
- Jickells, T. D., Boyd, S. S., & Knap, A. H. (1988). Iodine cycling in the Sargasso Sea and the Bermuda inshore waters. *Marine Chemistry*, 24(1), 61–82. https://doi.org/10.1016/0304-4203(88)90006-0
- Jones, M. R., Chance, R., Dadic, R., Hannula, H. R., May, R., Ward, M., & Carpenter, L. J. (2023). Environmental iodine speciation quantification in seawater and snow using ion exchange chromatography and UV spectrophotometric detection. *Analytica Chimica Acta*, 1239, 340700. https://doi.org/10.1016/J.ACA.2022.340700
- Karl, D. M., & Dore, J. E. (2001). Microbial ecology at sea: Sampling, subsampling and incubation considerations. *Methods in Microbiology*, *30*, 13–39. https://doi.org/10.1016/S0580-9517(01)30037-5
- Lu, Z., Jenkyns, H. C., & Rickaby, R. E. M. (2010). Iodine to calcium ratios in marine carbonate as a paleo-redox proxy during oceanic anoxic events. *Geology*, *38*(12), 1107–1110. https://doi.org/10.1130/G31145.1
- Luhar, A. K., Galbally, I. E., Woodhouse, M. T., & Thatcher, M. (2017). An improved parameterisation of ozone dry deposition to the ocean and its impact in a global climate-chemistry model. *Atmospheric Chemistry and Physics*, *17*(5), 3749–3767. https://doi.org/10.5194/ACP-17-3749-2017
- Luther, G. W. (2023). Review on the physical chemistry of iodine transformations in the oceans. *Frontiers in Marine Science*, *10*, 1085618. https://doi.org/10.3389/FMARS.2023.1085618/BIBTEX

- Miwa, K., Obata, H., & Suzuki, T. (2020). Vertical distributions of Iodine-129 and iodide in the Chukchi Sea and Bering Sea. *Journal of Nuclear Science and Technology*, *57*(5), 537–545. https://doi.org/10.1080/00223131.2019.1699189
- Moriyasu, R., Bolster, K. M., Hardisty, D. S., Kadko, D. C., Stephens, M. P., & Moffett, J. W. (2023). Meridional Survey of the Central Pacific Reveals Iodide Accumulation in Equatorial Surface Waters and Benthic Sources in the Abyssal Plain. *Global Biogeochemical Cycles*, 37(3), e2021GB007300. https://doi.org/10.1029/2021GB007300
- Moriyasu, R., Evans, N., Bolster, K. M., Hardisty, D. S., & Moffett, J. W. (2020). The Distribution and Redox Speciation of Iodine in the Eastern Tropical North Pacific Ocean. *Global Biogeochemical Cycles*, *34*(2), e2019GB006302. https://doi.org/10.1029/2019GB006302
- Qi, Y., Matsuzaki, H., Yamagata, T., & Nagai, H. (2023). Iodine cycling in the subarctic Pacific Ocean: Insights from 129I. *Geochimica et Cosmochimica Acta*, 344, 12–23. https://doi.org/10.1016/J.GCA.2023.01.006
- Rees, A. (2023). AMT30 Cruise Report. https://doi.org/10.17031/D2VS-EG36
- Rees, A., Robinson, C., Smyth, T., Aiken, J., Nightingale, P., & Zubkov, M. (2015). 20 years of the Atlantic Meridional Transect—AMT. *Limnology and Oceanography Bulletin*, 24(4), 101–107. https://doi.org/10.1002/LOB.10069
- Reifenhäuser, C., & Heumann, K. G. (1990). Development of a definitive method for iodine speciation in aquatic systems. *Fresenius' Journal of Analytical Chemistry*, *336*(7), 559–563. https://doi.org/10.1007/BF00331416/METRICS
- Schnur, A. A., Sutherland, K. M., Hansel, C. M., & Hardisty, D. S. (2023). Rates and pathways of iodine speciation transformations at the Bermuda Atlantic Time Series. *Frontiers in Marine Science*, *10*, 1272870. https://doi.org/10.3389/FMARS.2023.1272870/BIBTEX
- Spokes, L. J., & Liss, P. S. (1996). Photochemically induced redox reactions in seawater, II. Nitrogen and iodine. *Marine Chemistry*, 54(1–2), 1–10. https://doi.org/10.1016/0304-4203(96)00033-3
- Ştreangă, I. M., Repeta, D. J., Blusztajn, J. S., & Horner, T. J. (2023). Speciation and cycling of iodine in the subtropical North Pacific Ocean. *Frontiers in Marine Science*, *10*, 1272968. https://doi.org/10.3389/FMARS.2023.1272968/BIBTEX
- Tarran, G. A., Heywood, J. L., & Zubkov, M. V. (2006). Latitudinal changes in the standing stocks of nano- and picoeukaryotic phytoplankton in the Atlantic Ocean. *Deep Sea Research Part II: Topical Studies in Oceanography*, *53*(14–16), 1516–1529. https://doi.org/10.1016/J.DSR2.2006.05.004

- Tilstone, G. H., Lange, P. K., Misra, A., Brewin, R. J. W., & Cain, T. (2017). Microphytoplankton photosynthesis, primary production and potential export production in the Atlantic Ocean. *Progress in Oceanography*, *158*, 109–129. https://doi.org/10.1016/J.POCEAN.2017.01.006
- Truesdale, V. W., Bale, A. J., & Woodward, E. M. S. (2000). The meridional distribution of dissolved iodine in near-surface waters of the Atlantic Ocean. *Progress in Oceanography*, 45(3–4), 387–400. https://doi.org/10.1016/S0079-6611(00)00009-4
- Truesdale, V. W., Nausch, G., & Baker, A. (2001). The distribution of iodine in the Baltic Sea during summer. *Marine Chemistry*, 74(2–3), 87–98. https://doi.org/10.1016/S0304-4203(00)00115-8
- Veldhuis, M. J. W., & Timmermans, K. R. (2007). Phytoplankton dynamics during an in situ iron enrichment experiment (EisenEx) in the Southern Ocean: a comparative study of field and bottle incubation measurements. *Aquatic Microbial Ecology*, 47(2), 191–208. https://doi.org/10.3354/AME047191
- Wadley, M. R., Stevens, D. P., Jickells, T. D., Hughes, C., Chance, R., Hepach, H., Tinel, L., & Carpenter, L. J. (2020). A Global Model for Iodine Speciation in the Upper Ocean. *Global Biogeochemical Cycles*, 34(9), e2019GB006467. https://doi.org/10.1029/2019GB006467
- Wong, G. T. F., & Brewer, P. G. (1977). The marine chemistry of iodine in anoxic basins. Geochimica et Cosmochimica Acta, 41(1), 151–159. https://doi.org/10.1016/0016-7037(77)90195-8
- Wong, G. T. F., Piumsomboon, A. U., & Dunstan, W. M. (2002). The transformation of iodate to iodide in marine phytoplankton cultures. *Marine Ecology Progress Series*, 237, 27–39. https://doi.org/10.3354/MEPS237027
- Žic, V., & Branica, M. (2006). Iodate and Iodide Distributions in the Waters of a Stratified Estuary. *Croatica Chemica Acta*, 79(1), 143–153.

APPENDIX

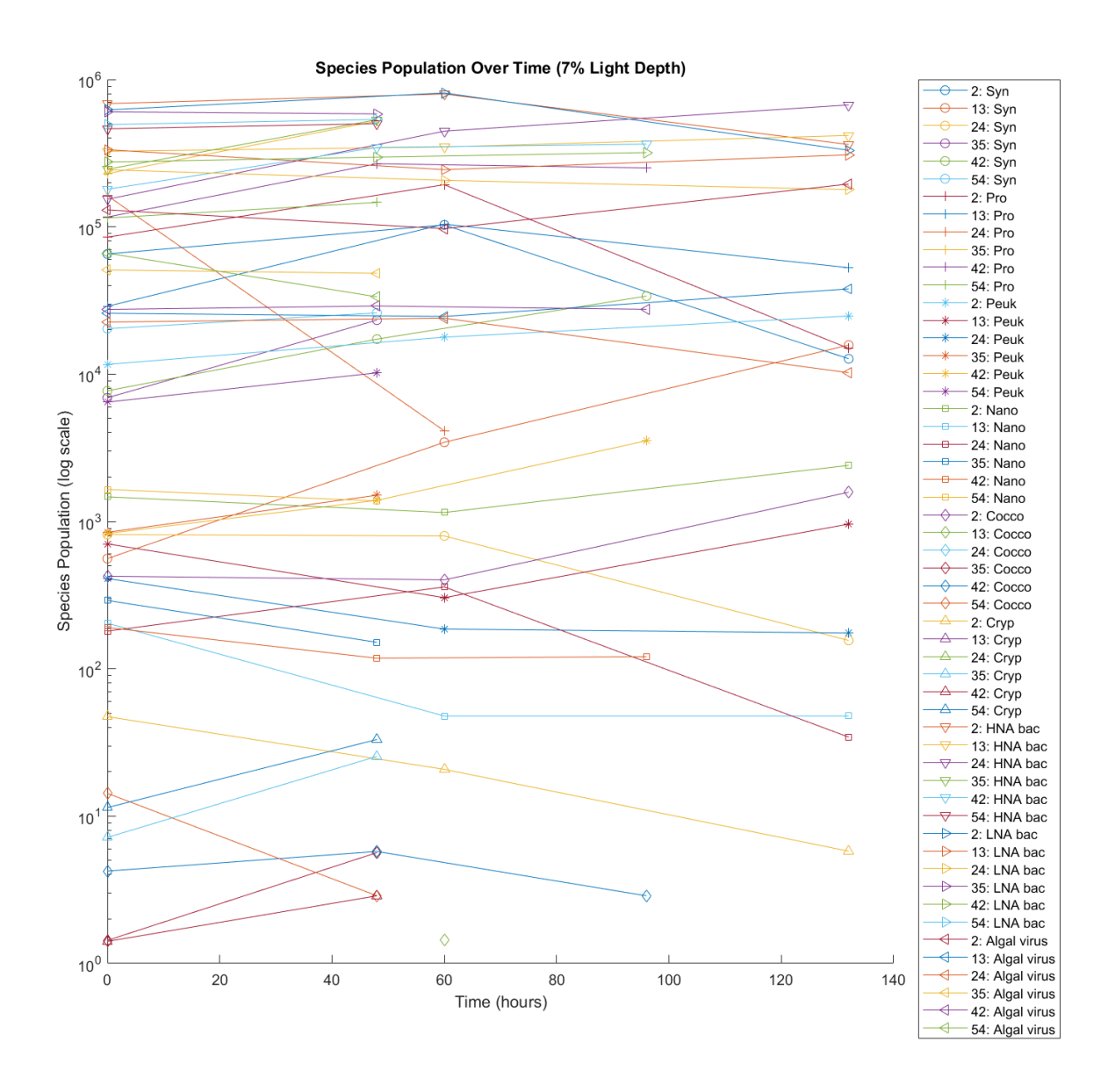


Figure S13: taxonomic analysis of shipboard incubations over time at the 7% light percentage for all stations.

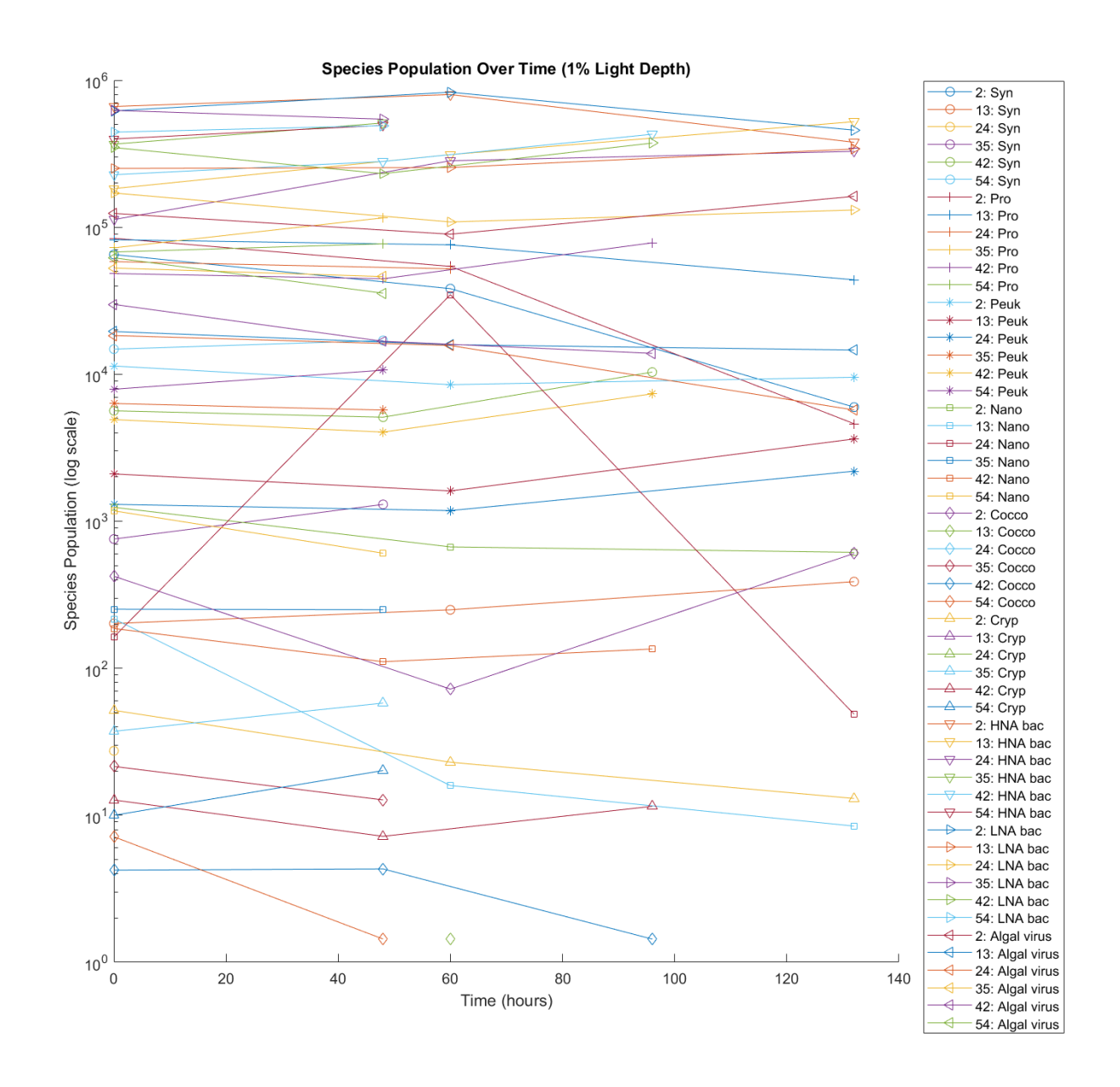


Figure S14: taxonomic analysis of shipboard incubations over time at the 1% light percentage for all stations.

Table S6. Isotope and Concentration Incubation Data Table.

							Iodide	Iodate		
Sample	Station			Depth	Date	Light	Concentration	Concentration	Iodide	Iodate
Number	Number	Latitude	Longitude	(m)	Collected	Percent	(nM)	(nM)	Ratio	Ratio
AMT30-		-	-							
22	2	45.30.206	47.49.736	15	2/23/2023	7%	260.2447936	510.290974	0.448735	0.007268
AMT30-		-	-							
23	2	45.30.206	47.49.736	15	2/23/2023	7%	264.1765011	471.5412281	0.448763	0.006568
AMT30-		-	-							
24	2	45.30.206	47.49.736	15	2/23/2023	7%	288.6021005	484.5922722	0.447111	0.006985
AMT30-	_	-	-							
125	2	45.30.206	47.49.736	15	3/1/2023	7%	268.8900081	503.1586409	0.44097	0.007094
AMT30-	2	-	-	1	2/1/2022	70/	204.0600726	60 7 0 2 05556	0.407.40.4	0.000515
126	2	45.30.206	47.49.736	15	3/1/2023	7%	294.0608726	607.0395556	0.437424	0.008515
AMT30-	2	-	-	1.5	2/1/2022	70/	202 4047505	500.041520	0.442026	0.000541
127	2	45.30.206	47.49.736	15	3/1/2023	7%	302.4847505	500.841738	0.443926	0.008541
AMT30-	2	- 45 20 20 <i>c</i>	- 47 40 726	20	2/22/2022	1.0/	202 000 4927	412 000052		0.006701
19 AMT30-	2	45.30.206	47.49.736	30	2/23/2023	1%	293.0994827	412.890952	-	0.006791
AM1130- 20	2	45.30.206	- 47.49.736	30	2/23/2023	1%	270.5157665	519.2421516	_	0.006034
AMT30-	2	45.30.200	47.49.730	30	2/23/2023	1 70	270.3137003	319.2421310	-	0.000034
21	2	45.30.206	47.49.736	30	2/23/2023	1%	204.4339316	366.7338982	_	0.006763
AMT30-	2	43.30.200	47.49.730	30	2/23/2023	1 70	204.4339310	300.7336962	-	0.000703
128	2	45.30.206	47.49.736	30	3/1/2023	1%	225.3930194	451.8544198	_	0.006845
AMT30-	2	-	-	30	3/1/2023	170	223.3730171	131.0311170		0.000015
129	2	45.30.206	47.49.736	30	3/1/2023	1%	210.9211709	371.0518945	_	0.006695
AMT30-	-	-	-	20	3, 1, 2023	170	210.7211707	271.02107.0		0.00000
130	2	45.30.206	47.49.736	30	3/1/2023	1%	282.3740137	378.7822378	_	0.007658
AMT30-	_	-38	-42		-, -, - 3 - 5	-,-				
107	7	27.109	45.511	30	2/26/2023	7%	197.2015611	297.4115876	0.398544	0.008533

Table S6 (cont'd)

AMT30-		-38	-42							
108	7	27.109	45.511	30	2/26/2023	7%	162.3002462	282.8564045	0.396083	0.009248
AMT30-		-38	-42							
109	7	27.109	45.511	30	2/26/2023	7%	299.7948955	483.2663869	0.400454	0.007889
AMT30-	_	-38	-42	•	2/1/2022				0.00.000	0.000.44
227	7	27.109	45.511	30	3/4/2023	7%	295.8774102	415.5059257	0.396092	0.00961
AMT30-	7	-38	-42	20	2/4/2022	70/	202 415226	406 5251004	0.205662	0.000010
228	7	27.109	45.511	30	3/4/2023	7%	292.415326	496.5351894	0.395662	0.008818
AMT30-	7	-38 27 100	-42	20	2/4/2022	70/	270 10524	106 6120020	0.202510	0.00070
229 AMT30-	7	27.109 -38	45.511 -42	30	3/4/2023	7%	279.19524	406.6429829	0.393519	0.008678
92	7	-36 27.109	-42 45.511	55	2/26/2023	1%	194.7087509	392.5636733	0.407883	0.010858
AMT30-	,	-38	-42	33	2/20/2023	1 /0	174.7007307	372.3030733	0.407003	0.010656
93	7	27.109	45.511	55	2/26/2023	1%	199.984966	379.2825418	0.409079	0.010342
AMT30-	,	-38	-42	33	2, 20, 2025	170	177.70 1700	377.2023 110	0.107077	0.010312
94	7	27.109	45.511	55	2/26/2023	1%	200.2781964	395.4713953	0.409104	0.011207
AMT30-		-38	-42							
140	7	27.109	45.511	55	3/1/2023	1%	187.3618448	416.0195554	0.406068	0.008225
AMT30-		-38	-42							
141	7	27.109	45.511	55	3/1/2023	1%	188.0085233	401.2668903	0.408183	0.009928
AMT30-		-38	-42							
142	7	27.109	45.511	55	3/1/2023	1%	202.2166579	416.5051495	-	0.008578
AMT30-		-38	-42							
212	7	27.109	45.511	55	3/4/2023	1%	181.2209247	417.585739	0.402023	0.011915
AMT30-	_	-38	-42		0/4/0000	10/	155 51 50 5 65	442 251 255	0.404407	0.011770
213	7	27.109	45.511	55	3/4/2023	1%	177.7150567	442.3518558	0.404187	0.011779
AMT30-	7	-38 27 100	-42	<i></i>	2/4/2022	10/	170 6700615	202 2112200	0.200575	0.011740
214	7	27.109	45.511	55	3/4/2023	1%	178.6708615	393.3113209	0.399575	0.011748
AMT30-	12	-33 16 405	-33	60	2/1/2022	70/	266 7271 455	171 7006661	0.2010	0.006054
179	13	16.405	20.230	60	3/1/2023	7%	266.7271455	471.7226661	0.3819	0.006954

Table S6 (cont'd)

AMT30-		-33	-33							
180	13	16.405	20.230	60	3/1/2023	7%	304.4036475	437.1143962	0.382848	0.006627
AMT30-		-33	-33							
181	13	16.405	20.230	60	3/1/2023	7%	472.4012408	453.0971069	0.370536	0.00735
AMT30-		-33	-33							
311	13	16.405	20.230	60	3/7/2023	7%	293.5024343	488.7566029	0.378318	0.007137
AMT30-		-33	-33							
312	13	16.405	20.230	60	3/7/2023	7%	294.2321685	457.4221336	0.381613	0.006956
AMT30-		-33	-33							
313	13	16.405	20.230	60	3/7/2023	7%	276.3529759	450.8738722	0.375867	0.007196
AMT30-	10	-33	-33	105	0.11.10.000	10/	101 70 ((100	440.000050		0.044500
182	13	16.405	20.230	105	3/1/2023	1%	181.5066429	410.802958	-	0.011709
AMT30-	10	-33	-33	105	2/1/2022	10/	15 6 05 10 40 4	412 2110125		0.010024
183	13	16.405	20.230	105	3/1/2023	1%	176.8512434	412.3119125	-	0.010034
AMT30-	10	-33	-33	105	2/1/2022	10/	176 4604002	120 5575005		0.010142
184	13	16.405	20.230	105	3/1/2023	1%	176.4694883	420.5575895	-	0.010142
AMT30-	13	-33 16.405	-33	105	3/4/2023	1.0/	145 2000127	256 5716792		0.010939
236	13	16.405 -33	20.230	105	3/4/2023	1%	145.2098137	356.5716783	-	0.010939
AMT30- 237	13	-33 16.405	-33 20.230	105	3/4/2023	1%	108.3098527	416.9477341		0.012062
AMT30-	13	-33	-33	103	3/4/2023	1 %	100.3090327	410.9477341	-	0.012002
238	13	-33 16.405	20.230	105	3/4/2023	1%	168.0720087	255.0942673		0.010983
AMT30-	13	-33	-33	103	3/4/2023	1 /0	100.0720007	233.0742073	_	0.010703
314	13	16.405	20.230	105	3/7/2023	1%	178.662573	436.4344637	_	0.009783
AMT30-	13	-33	-33	103	3/1/2023	170	170.002373	130.1311037		0.007703
315	13	16.405	20.230	105	3/7/2023	1%	179.3778515	418.6994922	_	0.009276
AMT30-	10	-33	-33	100	5, 1, 2028	170	17710770010	.10.000		0.0072.0
316	13	16.405	20.230	105	3/7/2023	1%	177.2043492	429.1932547	_	0.010658
AMT30-	-	-27	-24				· -	•		
290	19	18.821	31.421	75	3/4/2023	7%	219.8043346	333.0976498	-	0.007614

Table S6 (cont'd)

AMT30-		-27	-24							
291	19	18.821	31.421	75	3/4/2023	7%	223.4817582	317.6105979	-	0.00874
AMT30-		-27	-24							
292	19	18.821	31.421	75	3/4/2023	7%	226.8743051	348.5816352	-	0.00875
AMT30-		-27	-24							
341	19	18.821	31.421	75	3/7/2023	7%	222.5167207	317.5888125	-	-
AMT30-		-27	-24							
342	19	18.821	31.421	75	3/7/2023	7%	158.03536	353.9280675	-	-
AMT30-		-27	-24							
343	19	18.821	31.421	75	3/7/2023	7%	232.0255691	234.9266021	-	-
AMT30-		-27	-24							
404	19	18.821	31.421	75	3/10/2023	7%	227.0071005	333.2925576	-	0.007386
AMT30-		-27	-24							
405	19	18.821	31.421	75	3/10/2023	7%	223.6384934	349.3093398	-	0.008976
AMT30-		-27	-24							
406	19	18.821	31.421	75	3/10/2023	7%	232.0501975	326.7334223	-	0.008174
AMT30-		-27	-24							
278	19	18.821	31.421	105	3/4/2023	1%	217.8025707	548.0970721	0.296021	0.032082
AMT30-		-27	-24							
279	19	18.821	31.421	105	3/4/2023	1%	204.4916929	511.4473072	0.311532	0.032781
AMT30-		-27	-24							
280	19	18.821	31.421	105	3/4/2023	1%	165.0449045	468.3220803	0.374194	0.037094
AMT30-		-27	-24							
392	19	18.821	31.421	105	3/10/2023	1%	186.3777868	505.9335726	-	0.030644
AMT30-		-27	-24							
393	19	18.821	31.421	105	3/10/2023	1%	199.4679277	563.8097405	-	0.029897
AMT30-		-27	-24							
394	19	18.821	31.421	105	3/10/2023	1%	136.5238653	546.2605335	-	0.040504
AMT30-										
362	24	-18 1.386	-25 3.809	100	3/7/2023	7%	250.643644	326.7767926	-	0.007752

Table S6 (cont'd)

AMT30-										
363	24	-18 1.386	-25 3.809	100	3/7/2023	7%	262.3485753	319.1896309	-	0.006575
AMT30-										
364	24	-18 1.386	-25 3.809	100	3/7/2023	7%	276.5803411	304.9068303	-	0.007283
AMT30-										
413	24	-18 1.386	-25 3.809	100	3/10/2023	7%	267.9001507	323.6959804	-	-
AMT30-										
414	24	-18 1.386	-25 3.809	100	3/10/2023	7%	267.8175761	319.2334884	-	-
AMT30-										
415	24	-18 1.386	-25 3.809	100	3/10/2023	7%	278.3058331	328.3603633	-	-
AMT30-										
491	24	-18 1.386	-25 3.809	100	3/13/2023	7%	262.1971471	303.1227845	-	0.007317
AMT30-					- / - /					
492	24	-18 1.386	-25 3.809	100	3/13/2023	7%	274.9247797	312.2251524	-	0.007965
AMT30-	2.4	10.1.206	25.2.000	100	2/12/2022	70/	271 0651020	204 50 60 572		0.00005
493	24	-18 1.386	-25 3.809	100	3/13/2023	7%	271.0651038	304.5969572	-	0.00905
AMT30-	2.4	10 1 206	25 2 000	155	2/7/2022	1.07	204 1617254	470 2220104	0.246001	0.045462
365	24	-18 1.386	-25 3.809	155	3/7/2023	1%	204.1617254	479.3239184	0.346091	0.045463
AMT30- 366	24	-18 1.386	-25 3.809	155	3/7/2023	1.0/	219.9865367	432.5807416	0.332578	0.040257
300 AMT30-	24	-18 1.380	-23 3.809	133	3/1/2023	1%	219.9803307	432.3807410	0.332378	0.040237
367	24	-18 1.386	-25 3.809	155	3/7/2023	1%	216.8592608	512.8884861	0.328483	0.045586
AMT30-	24	-10 1.300	-23 3.607	133	3/1/2023	1 /0	210.0372000	312.0004001	0.320403	0.043300
494	24	-18 1.386	-25 3.809	155	3/13/2023	1%	244.5644962	501.6719277	0.30216	0.028549
AMT30-	21	10 1.500	23 3.007	133	3/13/2023	170	211.5011502	301.0717277	0.30210	0.020317
495	24	-18 1.386	-25 3.809	155	3/13/2023	1%	253.7960099	485.7912514	0.31422	0.026648
AMT30-		10 1.000	20 0.007	100	0,10,2020	1,0	2001.700077	.001// 1201 .	0.01.22	0.0200.0
496	24	-18 1.386	-25 3.809	155	3/13/2023	1%	207.8367	453.2195797	0.344479	0.090772
AMT30-					_					
470	30	-8 44.641	-25 9.408	90	3/10/2023	7%	309.4456343	292.2099688	-	0.010282

Table S6 (cont'd)

ANTE										
AMT30- 471	30	-8 44.641	-25 9.408	90	3/10/2023	7%	322.8031111	291.6109794	_	0.009365
AMT30-	30	0 44.041	23 7.400	70	3/10/2023	7 70	322.0031111	271.0107774		0.007303
472	30	-8 44.641	-25 9.408	90	3/10/2023	7%	330.8055461	283.971993	-	0.009158
AMT30-										
521	30	-8 44.641	-25 9.408	90	3/13/2023	7%	315.4916437	280.7693119	-	-
AMT30-										
522	30	-8 44.641	-25 9.408	90	3/13/2023	7%	326.9176749	305.1717479	-	-
AMT30-	20	0.44.644	27.0.400	0.0	2/12/2022	= 0.4	220 1017 (2	277 2777004		
523	30	-8 44.641	-25 9.408	90	3/13/2023	7%	320.4047662	275.2575884	-	-
AMT30- 584	30	-8 44.641	-25 9.408	90	3/15/2023	7%	339.124471	278.5821862		0.008959
304 AMT30-	30	-6 44.041	-23 9.406	90	3/13/2023	7 %0	339.1244/1	270.3021002	-	0.008939
585	30	-8 44.641	-25 9.408	90	3/15/2023	7%	331.5536678	277.5196631	_	0.009681
AMT30-	30	0 11.011	23 7.100	70	3/13/2023	7 70	331.3330070	277.5170051		0.007001
586	30	-8 44.641	-25 9.408	90	3/15/2023	7%	333.9197946	280.417484	_	0.010006
AMT30-										
458	30	-8 44.641	-25 9.408	110	3/10/2023	1%	204.7929015	416.5822333	-	0.009468
AMT30-										
459	30	-8 44.641	-25 9.408	110	3/10/2023	1%	228.7554842	532.2490894	-	0.009078
AMT30-										
460	30	-8 44.641	-25 9.408	110	3/10/2023	1%	212.6326222	569.3654745	-	0.009456
AMT30-	20	0 44 641	25.0.409	110	2/15/2022	1.0/	220 470000	200 2722414		0.000005
572 AMT30-	30	-8 44.641	-25 9.408	110	3/15/2023	1%	220.479988	280.2733414	-	0.008995
573	30	-8 44.641	-25 9.408	110	3/15/2023	1%	320.2936336	345.1897108	_	0.009519
AMT30-	30	-0 44.041	-23 7.400	110	3/13/2023	1 /0	320.2730330	343.107/100	_	0.007317
574	30	-8 44.641	-25 9.408	110	3/15/2023	1%	348.0903144	297.2444223	_	0.01081
AMT30-	20	5 5 . 1	-25		2. 10. 2020	1,0	2			3.01001
542	35	0 55.755	22.639	40	3/13/2023	7%	281.2195961	321.4670019	0.3124	0.013156

Table S6 (cont'd)

AMT30-			-25							
543	35	0 55.755	22.639	40	3/13/2023	7%	286.064345	339.0490165	0.312143	0.014571
AMT30-			-25							
544	35	0 55.755	22.639	40	3/13/2023	7%	289.2681293	353.5077996	0.312311	0.013604
AMT30-			-25							
593	35	0 55.755	22.639	40	3/15/2023	7%	291.7820399	353.9635641	-	-
AMT30-			-25							
594	35	0 55.755	22.639	40	3/15/2023	7%	282.3028757	340.8273462	-	-
AMT30-	a -	^ -	-25	4.0	0.4.7.40000		•••	. 		
595	35	0 55.755	22.639	40	3/15/2023	7%	292.0091977	344.6774606	-	-
AMT30-	25	0.55.755	-25	40	2/17/2022	70/	272 1101770	222 4269595	0.210400	0.015704
671 AMT30-	35	0 55.755	22.639 -25	40	3/17/2023	7%	272.1101778	323.4268585	0.310499	0.015704
672	35	0 55.755	-23 22.639	40	3/17/2023	7%	277.5984909	343.3063652	0.310762	0.016331
AMT30-	33	0 33.733	-25	40	3/11/2023	7 %	211.3904909	343.3003032	0.310702	0.010331
673	35	0 55.755	22.639	40	3/17/2023	7%	290.3817934	333.2289782	0.310382	0.015351
AMT30-	33	0 33.133	-25	10	3/17/2023	7 70	270.3017731	333.2207102	0.310302	0.015551
545	35	0 55.755	22.639	65	3/13/2023	1%	154.7346643	556.3014499	0.318209	0.026094
AMT30-			-25							
546	35	0 55.755	22.639	65	3/13/2023	1%	170.1156429	433.8380253	0.309215	0.023821
AMT30-			-25							
547	35	0 55.755	22.639	65	3/13/2023	1%	173.1920337	673.7860757	0.308056	0.024734
AMT30-			-25							
674	35	0 55.755	22.639	65	3/17/2023	1%	191.3765479	279.3275635	0.313839	0.011992
AMT30-			-25							
675	35	0 55.755	22.639	65	3/17/2023	1%	198.512993	269.2465135	0.288893	0.013767
AMT30-			-25							
676	35	0 55.755	22.639	65	3/17/2023	1%	257.6490219	415.083892	0.324299	0.012895
AMT30-	4.1	10.07.070	-25	40	0.11.6.100.000	7 01	225 5102521	246.0070265		0.015.425
650	41	10 25.350	17.460	40	3/16/2023	7%	235.5183531	346.8870366	-	0.015425

Table S6 (cont'd)

AMT30-			-25							
651	41	10 25.350	17.460	40	3/16/2023	7%	218.064137	343.9992847	-	0.014113
AMT30-			-25							
652	41	10 25.350	17.460	40	3/16/2023	7%	247.7894914	340.4448662	-	0.01363
AMT30-			-25							
701	41	10 25.350	17.460	40	3/18/2023	7%	231.4652796	335.1430039	-	-
AMT30-	4.4	10.27.270	-25	40	0.410.40000	= 0.4	225 5255210	221 7007 402		
702	41	10 25.350	17.460	40	3/18/2023	7%	235.7275318	331.5805693	-	-
AMT30-	4.1	10.25.250	-25	40	2/10/2022	70/	225 0205200	222 5000 624		
703	41	10 25.350	17.460	40	3/18/2023	7%	237.8297388	332.5909624	-	-
AMT30- 764	41	10 25.350	-25 17.460	40	2/20/2022	70/	249 2225721	332.803988		0.013709
704 AMT30-	41	10 23.330	-25	40	3/20/2023	7%	248.2325731	332.803988	-	0.013709
765	41	10 25.350	-23 17.460	40	3/20/2023	7%	249.4557076	345.5251536		0.015904
AMT30-	41	10 23.330	-25	40	3/20/2023	7 70	249.4337070	343.3231330	-	0.013704
766	41	10 25.350	17.460	40	3/20/2023	7%	242.4297983	351.537048	_	0.012204
AMT30-	11	10 23.330	-25	10	3/20/2023	7 70	212.127703	331.337010		0.012201
638	41	10 25.350	17.460	60	3/16/2023	1%	196.3430516	337.8277636	_	0.016604
AMT30-			-25							
639	41	10 25.350	17.460	60	3/16/2023	1%	140.036773	245.9346001	_	0.023482
AMT30-			-25							
640	41	10 25.350	17.460	60	3/16/2023	1%	150.235214	350.1686031	-	0.01807
AMT30-			-25							
752	41	10 25.350	17.460	60	3/20/2023	1%	213.5968069	387.241937	0.462288	0.01141
AMT30-			-25							
753	41	10 25.350	17.460	60	3/20/2023	1%	167.6039221	367.2273527	0.46978	0.012619
AMT30-			-25							
754	41	10 25.350	17.460	60	3/20/2023	1%	192.2654783	241.239261	0.478388	0.012183
AMT30-			-24							
722	42	20 41.930	59.866	50	3/19/2023	7%	239.7037741	467.1950704	0.379517	0.05678

Table S6 (cont'd)

AMT30-			-24							
723	42	20 41.930	59.866	50	3/19/2023	7%	195.1676115	522.4551292	0.37757	0.070849
AMT30-			-24							
724	42	20 41.930	59.866	50	3/19/2023	7%	192.4290154	470.963653	0.377973	0.065271
AMT30-			-24							
773	42	20 41.930	59.866	50	3/21/2023	7%	119.2998448	514.7489662	-	-
AMT30-			-24							
774	42	20 41.930	59.866	50	3/21/2023	7%	133.3898873	504.8777816	-	-
AMT30-	4.0	20.44.020	-24	7 0	0/01/0000	= 0.4	100 (055.115	105 505 5050		
775	42	20 41.930	59.866	50	3/21/2023	7%	130.6377417	487.5256973	-	-
AMT30-	42	20 41 020	-24	50	2/22/2022	70/	125 0222027	470 7200742		0.070020
851 AMT30-	42	20 41.930	59.866 -24	50	3/23/2023	7%	125.0232037	479.7200742	-	0.078938
852	42	20 41.930	-2 4 59.866	50	3/23/2023	7%	135.2945405	511.4909122		0.07053
AMT30-	42	20 41.930	-24	30	3/23/2023	7 70	133.2943403	311.4909122	-	0.07033
853	42	20 41.930	59.866	50	3/23/2023	7%	143.3288601	455.3316909	_	0.064874
AMT30-	12	20 11.930	-24	30	3/23/2023	7 70	113.3200001	155.5510707		0.001071
725	42	20 41.930	59.866	85	3/19/2023	1%	244.4537203	245.9724014	0.403975	0.015425
AMT30-			-24		2, 2, 2, 2			,		
726	42	20 41.930	59.866	85	3/19/2023	1%	242.9473132	222.1257839	0.404279	0.015607
AMT30-			-24							
727	42	20 41.930	59.866	85	3/19/2023	1%	186.2659418	199.1920202	0.394888	0.016279
AMT30-			-24							
776	42	20 41.930	59.866	85	3/21/2023	1%	240.3378619	394.1953273	-	0.011158
AMT30-			-24							
777	42	20 41.930	59.866	85	3/21/2023	1%	273.3463323	388.4246628	-	0.010105
AMT30-			-24							
778	42	20 41.930	59.866	85	3/21/2023	1%	182.6037355	352.67773	-	0.010572
AMT30-		•0.44.055	-24	0.7	0 /00 /00 0	4	• • • • • • • • • • • • • • • • • • • •	211 00217-	0.40225=	0.00==1
854	42	20 41.930	59.866	85	3/23/2023	1%	267.6987397	311.0921576	0.403307	0.007516

Table S6 (cont'd)

AMT30-			-24							
855	42	20 41.930	59.866	85	3/23/2023	1%	237.7844436	334.6041763	0.404063	0.007363
AMT30-			-24							
856	42	20 41.930	59.866	85	3/23/2023	1%	261.5239973	333.9615982	0.405788	0.008924
AMT30-			-23							
830	48	29 16.323	40.649	55	3/22/2023	7%	86.24022413	514.6550275	0.442647	0.064838
AMT30-	40	20.45.222	-23		0.100.100.00	5 0/	55 1051 (552	550 10 55 010	0.442024	0.06060
831	48	29 16.323	40.649	55	3/22/2023	7%	77.10716772	552.1077919	0.442934	0.06069
AMT30-	40	20.16.222	-23	<i></i>	2/22/2022	70/	0.4.61.400002	070 5700054	0.440220	0.061500
832	48	29 16.323	40.649	55	3/22/2023	7%	84.61408993	870.5789054	0.440339	0.061509
AMT30- 881	48	29 16.323	-23 40.649	55	3/24/2023	7%	88.17920136	540.2074737		0.059588
AMT30-	40	29 10.323	-23	33	3/24/2023	7 70	00.17920130	340.2074737	-	0.039366
882	48	29 16.323	40.649	55	3/24/2023	7%	82.98419606	538.8301918	_	0.063085
AMT30-	40	27 10.323	-23	33	3/24/2023	7 70	02.70417000	330.0301710		0.003003
883	48	29 16.323	40.649	55	3/24/2023	7%	79.70707246	538.7106396	_	0.063577
AMT30-			-23							
944	48	29 16.323	40.649	55	3/26/2023	7%	88.94265277	534.9467417	-	0.061044
AMT30-			-23							
945	48	29 16.323	40.649	55	3/26/2023	7%	76.82949998	555.7828942	-	0.064622
AMT30-			-23							
946	48	29 16.323	40.649	55	3/26/2023	7%	50.67224049	422.9310099	-	0.069335
AMT30-			-23							
818	48	29 16.323	40.649	112	3/22/2023	1%	180.8051346	378.4554336	0.458659	0.010539
AMT30-			-23							
819	48	29 16.323	40.649	112	3/22/2023	1%	186.5830051	342.1936418	0.473565	0.011802
AMT30-	40	20.16.222	-23	110	2/22/2022	10/	170 1077027	242 00001 47	0.472000	0.011550
820	48	29 16.323	40.649	112	3/22/2023	1%	170.1077827	243.9998147	0.473098	0.011552
AMT30- 869	48	29 16.323	-23	112	3/24/2023	1.0/	120 2240649	450.721155		0.007429
809	48	29 10.323	40.649	112	3/24/2023	1%	139.2340648	430.721133	-	0.007429

Table S6 (cont'd)

AMT30-			-23							
870	48	29 16.323	40.649	112	3/24/2023	1%	213.9281681	476.3095109	-	0.007908
AMT30-			-23							
871	48	29 16.323	40.649	112	3/24/2023	1%	144.080203	486.9942775	-	0.008897
AMT30-			-23							
932	48	29 16.323	40.649	112	3/26/2023	1%	164.0334907	364.7638548	0.466946	0.007741
AMT30-	40	20.45.222	-23	110	0/0/2/0000	10/	104 500005	505.0105001	0.465010	0.005501
933	48	29 16.323	40.649	112	3/26/2023	1%	184.7383985	507.0105934	0.465219	0.005501
AMT30-	40	20.16.222	-23	110	2/26/2022	10/	104.0100.000	205.0266007	0.467001	0.006641
934	48	29 16.323	40.649	112	3/26/2023	1%	184.8189699	395.9366807	0.467801	0.006641
AMT30- 908	54	37 47.807	-18 46.836	20	3/25/2023	7%	153.4375867	483.6174437	0.618471	0.008332
AMT30-	34	37 47.607	-18	20	3/23/2023	7 70	133.4373607	403.0174437	0.0104/1	0.006332
909	54	37 47.807	46.836	20	3/25/2023	7%	168.2273609	501.1740741	0.617349	0.009508
AMT30-	54	37 47.007	-18	20	3/23/2023	7 70	100.2273007	301.1740741	0.017347	0.007300
910	54	37 47.807	46.836	20	3/25/2023	7%	164.0591144	463.7613201	0.615523	0.008582
AMT30-			-18		5, -5, -5-5				***************************************	
959	54	37 47.807	46.836	20	3/27/2023	7%	162.3529269	475.6752262	-	0.009363
AMT30-			-18							
960	54	37 47.807	46.836	20	3/27/2023	7%	176.1546889	471.8343468	-	0.009434
AMT30-			-18							
961	54	37 47.807	46.836	20	3/27/2023	7%	163.0654348	445.9671566	-	0.009003
AMT30-			-18							
905	54	37 47.807	46.836	25	3/25/2023	1%	148.5746521	371.67223	0.632255	0.007793
AMT30-			-18							
906	54	37 47.807	46.836	25	3/25/2023	1%	152.6004153	399.253768	0.634865	0.007145
AMT30-	~ .	25 45 005	-18	2.5	0/05/0000	10/	1.40.00.4000	20 < 4 < 2 + 2 = 2	0.600515	0.00
907	54	37 47.807	46.836	25	3/25/2023	1%	149.0842887	396.4624378	0.632517	0.00777
AMT30-	<i>5</i> 4	27 47 007	-18	25	2/27/2022	10/	155 0164077	550 1010747	0.507.63	0.006041
956	54	37 47.807	46.836	25	3/27/2023	1%	155.8164077	552.1910747	0.58763	0.006941

Table S6 (cont'd)

AMT30-			-18							
957	54	37 47.807	46.836	25	3/27/2023	1%	150.3109671	452.1089435	0.626313	0.006734
AMT30-			-18							
958	54	37 47.807	46.836	25	3/27/2023	1%	237.7421996	459.6713339	0.630342	0.006527

Table S7.
Depth Profile Data Table

Sampla	Station				Date	Iodide Concentration	Iodate Concentration
Sample Number	Number	Latitude	Longitude	Depth (m)	Collected	(nM)	(nM)
AMT30-27	2	-45.30.206	-47.49.736	200	2/23/2023	7.8592	231.3870
AMT30-28	2	-45.30.206	-47.49.736	150	2/23/2023	11.8598	205.0724
AMT30-29	2	-45.30.206	-47.49.736	100	2/23/2023	24.6794	342.9972
AMT30-30	2	-45.30.206	-47.49.736	60	2/23/2023	36.8399	313.0530
AMT30-31	$\frac{\overline{}}{2}$	-45.30.206	-47.49.736	40	2/23/2023	33.9740	132.4804
AMT30-32	2	-45.30.206	-47.49.736	30	2/23/2023	37.7876	193.2762
AMT30-33	2	-45.30.206	-47.49.736	25	2/23/2023	39.8927	213.2390
AMT30-34	2	-45.30.206	-47.49.736	20	2/23/2023	46.4915	227.7574
AMT30-35	2	-45.30.206	-47.49.736	15	2/23/2023	38.3279	184.2022
AMT30-36	2	-45.30.206	-47.49.736	5	2/23/2023	62.8146	252.2572
AMT30-110	7	-38 27.109	-42 45.511	5	2/26/2023	34.2836	248.9618
AMT30-111	7	-38 27.109	-42 45.511	10	2/26/2023	29.7368	177.3307
AMT30-112	7	-38 27.109	-42 45.511	15	2/26/2023	19.6803	134.5267
AMT30-113	7	-38 27.109	-42 45.511	25	2/26/2023	28.4812	199.1694
AMT30-114	7	-38 27.109	-42 45.511	30	2/26/2023	41.9868	278.6625
AMT30-115	7	-38 27.109	-42 45.511	50	2/26/2023	16.7888	138.0209
AMT30-116	7	-38 27.109	-42 45.511	55	2/26/2023	23.9124	193.9281
AMT30-117	7	-38 27.109	-42 45.511	80	2/26/2023	5.5656	303.9954
AMT30-118	7	-38 27.109	-42 45.511	100	2/26/2023	3.6525	144.1358
AMT30-119	7	-38 27.109	-42 45.511	150	2/26/2023	2.1657	172.0894
AMT30-120	7	-38 27.109	-42 45.511	250	2/26/2023	0.1519	215.7669
AMT30-121	7	-38 27.109	-42 45.511	500	2/26/2023	below detection	191.3075
AMT30-188	13	-33 16.405	-33 20.230	5	3/1/2023	66.9731	121.4460
AMT30-189	13	-33 16.405	-33 20.230	10	3/1/2023	80.4852	271.6965
AMT30-190	13	-33 16.405	-33 20.230	20	3/1/2023	83.5826	277.1460
AMT30-191	13	-33 16.405	-33 20.230	60	3/1/2023	76.0958	281.0385
AMT30-192	13	-33 16.405	-33 20.230	80	3/1/2023	65.8304	299.7225

Table S7 (cont'd)

AMT30-193	13	-33 16.405	-33 20.230	105	3/1/2023	57.0828	319.9635
AMT30-194	13	-33 16.405	-33 20.230	120	3/1/2023	33.9546	329.3055
AMT30-195	13	-33 16.405	-33 20.230	130	3/1/2023	23.4802	349.5465
AMT30-196	13	-33 16.405	-33 20.230	150	3/1/2023	15.3620	361.2240
AMT30-197	13	-33 16.405	-33 20.230	250	3/1/2023	3.3039	332.4195
AMT30-198	13	-33 16.405	-33 20.230	400	3/1/2023	below detection	375.2370
AMT30-199	13	-33 16.405	-33 20.230	500	3/1/2023	below detection	398.5920
AMT30-296	19	-27 18.821	-24 31.421	5	3/4/2023	97.4748	238.2881
AMT30-297	19	-27 18.821	-24 31.421	20	3/4/2023	105.1076	285.6497
AMT30-298	19	-27 18.821	-24 31.421	40	3/4/2023	105.0808	269.3691
AMT30-299	19	-27 18.821	-24 31.421	75	3/4/2023	63.4394	216.8273
AMT30-300	19	-27 18.821	-24 31.421	90	3/4/2023	70.2487	278.2494
AMT30-301	19	-27 18.821	-24 31.421	105	3/4/2023	54.9979	325.6110
AMT30-302	19	-27 18.821	-24 31.421	115	3/4/2023	43.1197	343.3716
AMT30-303	19	-27 18.821	-24 31.421	150	3/4/2023	21.8477	371.4926
AMT30-304	19	-27 18.821	-24 31.421	175	3/4/2023	14.1811	270.8492
AMT30-305	19	-27 18.821	-24 31.421	250	3/4/2023	below detection	396.6534
AMT30-306	19	-27 18.821	-24 31.421	400	3/4/2023	below detection	276.0293
AMT30-307	19	-27 18.821	-24 31.421	500	3/4/2023	below detection	339.6715
AMT30-371	24	-18 1.386	-25 3.809	5	3/7/2023	111.9028	226.3803
AMT30-372	24	-18 1.386	-25 3.809	10	3/7/2023	114.9350	168.2347
AMT30-373	24	-18 1.386	-25 3.809	20	3/7/2023	110.7383	198.4704
AMT30-374	24	-18 1.386	-25 3.809	40	3/7/2023	120.3928	202.3468
AMT30-375	24	-18 1.386	-25 3.809	80	3/7/2023	100.1160	206.9984
AMT30-376	24	-18 1.386	-25 3.809	100	3/7/2023	98.5091	223.2792
AMT30-377	24	-18 1.386	-25 3.809	155	3/7/2023	81.4681	259.7171
AMT30-378	24	-18 1.386	-25 3.809	170	3/7/2023	70.2235	218.6276
AMT30-379	24	-18 1.386	-25 3.809	185	3/7/2023	35.5711	334.1435
AMT30-380	24	-18 1.386	-25 3.809	250	3/7/2023	below detection	214.7512
AMT30-381	24	-18 1.386	-25 3.809	400	3/7/2023	below detection	262.8182
AMT30-382	24	-18 1.386	-25 3.809	500	3/7/2023	below detection	258.1666

Table S7 (cont'd)

AMT30-476	30	-8 44.641	-25 9.408	5	3/10/2023	90.2755	209.3520
AMT30-477	30	-8 44.641	-25 9.408	10	3/10/2023	119.0676	300.9435
AMT30-478	30	-8 44.641	-25 9.408	20	3/10/2023	123.1580	221.3461
AMT30-479	30	-8 44.641	-25 9.408	40	3/10/2023	113.6844	221.3461
AMT30-480	30	-8 44.641	-25 9.408	80	3/10/2023	145.2416	256.2381
AMT30-481	30	-8 44.641	-25 9.408	90	3/10/2023	129.6400	279.1360
AMT30-482	30	-8 44.641	-25 9.408	110	3/10/2023	123.3148	248.6055
AMT30-483	30	-8 44.641	-25 9.408	140	3/10/2023	58.7814	307.4858
AMT30-484	30	-8 44.641	-25 9.408	180	3/10/2023	3.8708	409.9810
AMT30-485	30	-8 44.641	-25 9.408	250	3/10/2023	below detection	558.2720
AMT30-486	30	-8 44.641	-25 9.408	400	3/10/2023	below detection	455.7768
AMT30-487	30	-8 44.641	-25 9.408	500	3/10/2023	below detection	450.3249
AMT30-551	35	0 55.755	-25 22.639	5	3/13/2023	110.1208	259.5560
AMT30-552	35	0 55.755	-25 22.639	10	3/13/2023	102.7148	249.2328
AMT30-553	35	0 55.755	-25 22.639	20	3/13/2023	115.7234	240.3843
AMT30-554	35	0 55.755	-25 22.639	40	3/13/2023	84.8337	184.3438
AMT30-555	35	0 55.755	-25 22.639	65	3/13/2023	90.5413	321.4955
AMT30-556	35	0 55.755	-25 22.639	80	3/13/2023	18.1852	308.2228
AMT30-557	35	0 55.755	-25 22.639	100	3/13/2023	5.0411	296.4248
AMT30-558	35	0 55.755	-25 22.639	120	3/13/2023	4.4094	379.0108
AMT30-559	35	0 55.755	-25 22.639	180	3/13/2023	2.3908	404.0815
AMT30-560	35	0 55.755	-25 22.639	250	3/13/2023	0.5083	389.3340
AMT30-561	35	0 55.755	-25 22.639	400	3/13/2023	below detection	387.8593
AMT30-562	35	0 55.755	-25 22.639	500	3/13/2023	below detection	411.4553
AMT30-656	41	10 25.350	-25 17.460	5	3/16/2023	151.6562	187.6500
AMT30-657	41	10 25.350	-25 17.460	10	3/16/2023	121.7976	200.1600
AMT30-658	41	10 25.350	-25 17.460	20	3/16/2023	137.6765	209.8900
AMT30-659	41	10 25.350	-25 17.460	40	3/16/2023	148.1032	254.3700
AMT30-660	41	10 25.350	-25 17.460	60	3/16/2023	76.3756	240.4700
AMT30-661	41	10 25.350	-25 17.460	70	3/16/2023	37.8211	272.4400
AMT30-662	41	10 25.350	-25 17.460	80	3/16/2023	27.0972	283.5600

Table S7 (cont'd)

AMT30-663	41	10 25.350	-25 17.460	100	3/16/2023	12.7583	395.4550
AMT30-664	41	10 25.350	-25 17.460	150	3/16/2023	0.5706	305.8000
AMT30-665	41	10 25.350	-25 17.460	250	3/16/2023	below detection	369.7400
AMT30-666	41	10 25.350	-25 17.460	400	3/16/2023	below detection	421.1700
AMT30-667	41	10 25.350	-25 17.460	500	3/16/2023	below detection	317.6150
AMT30-731	42	20 41.930	-24 59.866	5	3/19/2023	112.5670	336.7068
AMT30-732	42	20 41.930	-24 59.866	10	3/19/2023	120.0297	363.2701
AMT30-733	42	20 41.930	-24 59.866	20	3/19/2023	129.7545	341.7323
AMT30-734	42	20 41.930	-24 59.866	40	3/19/2023	142.7934	350.3474
AMT30-735	42	20 41.930	-24 59.866	50	3/19/2023	121.3852	363.2701
AMT30-736	42	20 41.930	-24 59.866	85	3/19/2023	127.7853	338.8606
AMT30-737	42	20 41.930	-24 59.866	110	3/19/2023	24.9442	492.4966
AMT30-738	42	20 41.930	-24 59.866	150	3/19/2023	7.0165	251.2738
AMT30-739	42	20 41.930	-24 59.866	200	3/19/2023	0.7517	482.4456
AMT30-740	42	20 41.930	-24 59.866	250	3/19/2023	-2.7918	493.9324
AMT30-741	42	20 41.930	-24 59.866	400	3/19/2023	-2.4289	557.1098
AMT30-742	42	20 41.930	-24 59.866	500	3/19/2023	-3.6925	580.8013
AMT30-836	48	29 16.323	-23 40.649	5	3/22/2023	60.6759	217.8008
AMT30-837	48	29 16.323	-23 40.649	10	3/22/2023	69.9225	315.7380
AMT30-838	48	29 16.323	-23 40.649	25	3/22/2023	64.9685	236.8035
AMT30-839	48	29 16.323	-23 40.649	55	3/22/2023	66.6261	236.8035
AMT30-840	48	29 16.323	-23 40.649	70	3/22/2023	42.8256	152.0220
AMT30-841	48	29 16.323	-23 40.649	112	3/22/2023	51.0814	217.8008
AMT30-842	48	29 16.323	-23 40.649	120	3/22/2023	99.5556	329.6246
AMT30-843	48	29 16.323	-23 40.649	135	3/22/2023	71.5454	264.5768
AMT30-844	48	29 16.323	-23 40.649	175	3/22/2023	16.3346	340.5878
AMT30-845	48	29 16.323	-23 40.649	250	3/22/2023	4.0095	358.1288
AMT30-846	48	29 16.323	-23 40.649	400	3/22/2023	4.4466	396.1343
AMT30-847	48	29 16.323	-23 40.649	500	3/22/2023	2.5303	384.4403
AMT30-911	54	37 47.807	-18 46.836	5	3/25/2023	32.6585	289.5743
AMT30-912	54	37 47.807	-18 46.836	10	3/25/2023	43.1305	373.0355

Table S7 (cont'd)

AMT30-913	54	37 47.807	-18 46.836	20	3/25/2023	37.4799	375.9385
AMT30-914	54	37 47.807	-18 46.836	25	3/25/2023	35.3955	354.1660
AMT30-915	54	37 47.807	-18 46.836	40	3/25/2023	32.0979	314.9755
AMT30-916	54	37 47.807	-18 46.836	50	3/25/2023	44.0385	373.7613
AMT30-917	54	37 47.807	-18 46.836	90	3/25/2023	37.9873	367.2295
AMT30-918	54	37 47.807	-18 46.836	120	3/25/2023	15.0614	351.2630
AMT30-919	54	37 47.807	-18 46.836	175	3/25/2023	-1.7071	444.1590
AMT30-920	54	37 47.807	-18 46.836	250	3/25/2023	-1.0047	418.0320
AMT30-921	54	37 47.807	-18 46.836	400	3/25/2023	-3.0342	448.5135
AMT30-922	54	37 47.807	-18 46.836	500	3/25/2023	-2.6350	431.0955